

1.0

1.1

1.25

3.2  
3.6  
4.0

2.8

3.2

3.6

4.0

2.5

2.2

2.0

1.8

1.4

1.6

**DTIC FILE COPY**

**Naval Research Laboratory**

Washington, DC 20375-5000



NRL Memorandum Report 6113

**AD-A189 079**

**Wavenumber — Frequency Structure of Turbulent Flow in a Channel from a Direct Simulation**

R. A. HANDLER

*Laboratory for Computational Physics and Fluid Dynamics*

November 30, 1987

**DTIC**  
**ELECTE**  
DEC 21 1987  
**S** **D**  
E

Approved for public release; distribution unlimited.

**87 12 16 100**

SECURITY CLASSIFICATION OF THIS PAGE

REPORT DOCUMENTATION PAGE				Form Approved OMB No 0704 0188	
1a REPORT SECURITY CLASSIFICATION UNCLASSIFIED		1b RESTRICTIVE MARKINGS			
2a SECURITY CLASSIFICATION AUTHORITY		3 DISTRIBUTION AVAILABILITY OF REPORT Approved for public release; distribution unlimited.			
2b DECLASSIFICATION/DOWNGRADING SCHEDULE					
4 PERFORMING ORGANIZATION REPORT NUMBER(S) NRL Memorandum Report 6113		5 MONITORING ORGANIZATION REPORT NUMBER(S)			
6a NAME OF PERFORMING ORGANIZATION Naval Research Laboratory	6b OFFICE SYMBOL (If applicable) Code 4420	7a NAME OF MONITORING ORGANIZATION			
6c ADDRESS (City, State, and ZIP Code) Washington, DC 20375-5000		7b ADDRESS (City, State, and ZIP Code)			
8a NAME OF FUNDING/SPONSORING ORGANIZATION Office of Naval Research	8b OFFICE SYMBOL (If applicable)	9 PROCUREMENT INSTRUMENT IDENTIFICATION NUMBER			
8c ADDRESS (City, State, and ZIP Code) Arlington, VA 22217		10 SOURCE OF FUNDING NUMBERS			
		PROGRAM ELEMENT NO 61153N	PROJECT NO	TASK NO RR023-01-41	WORK UNIT ACCESSION NO DN880-019
11 TITLE (Include Security Classification) Wavenumber-Frequency Structure of Turbulent Flow in a Channel from a Direct Simulation					
12 PERSONAL AUTHOR(S) R.A. Handler					
13a TYPE OF REPORT Interim	13b TIME COVERED FROM 3/86 TO 3/87	14 DATE OF REPORT (Year, Month, Day) 1987 November 30	15 PAGE COUNT 50		
16 SUPPLEMENTARY NOTATION					
17 COSATI CODES		18 SUBJECT TERMS (Continue on reverse if necessary and identify by block number)			
FIELD	GROUP	SUB GROUP	Turbulence Simulation		
19 ABSTRACT (Continue on reverse if necessary and identify by block number)					
<p>The detailed wavenumber-frequency structure of the streamwise and wall-normal components of the turbulent velocity has been obtained from a direct simulation in a channel. The turbulence is in an early stage of development but the features of the flow are qualitatively similar to the structure of fully developed turbulence. It is found from spectra computed in horizontal planes that wave speeds very near the wall are significantly higher than the local mean velocity and that the near wall streamwise velocity spectra exhibit a periodic structure. The spanwise length scale of this structure appears to correspond with the well known streak spacing observed in experiments. Detailed results of the wall pressure field reveal features which correspond closely with experiments in fully developed turbulence. Along with spectra obtained in the horizontal plane, the dependence of the correlations of wall-normal component of the turbulence on distance from the wall is presented. These correlations are directly related to a dominant source of wall pressure fluctuations.</p>					
20 DISTRIBUTION AVAILABILITY OF ABSTRACT <input checked="" type="checkbox"/> UNCLASSIFIED UNLIMITED <input type="checkbox"/> SAME AS RPT <input type="checkbox"/> DTIC USERS		21 ABSTRACT SECURITY CLASSIFICATION UNCLASSIFIED			
22a NAME OF RESPONSIBLE INDIVIDUAL Robert A. Handler		22b TELEPHONE (Include Area Code) (202) 767-2457	22c OFFICE SYMBOL Code 4420		

DD Form 1473, JUN 86

Previous editions are obsolete

SECURITY CLASSIFICATION OF THIS PAGE

S/N 0102-LF-014-6603

## CONTENTS

1. INTRODUCTION .....	1
2. COMPUTATIONAL PARAMETERS AND DATA ANALYSIS .....	3
3. RESULTS .....	6
4. SUMMARY AND CONCLUSIONS .....	16
ACKNOWLEDGEMENTS .....	17
REFERENCES .....	18

Accession For	
NTIS GRA&I	<input checked="" type="checkbox"/>
DTIC TAB	<input type="checkbox"/>
Unannounced	<input type="checkbox"/>
Justification	
By _____	
Distribution/	
Availability Codes	
Dist	Avail and/or Special
A-1	

# WAVENUMBER — FREQUENCY STRUCTURE OF TURBULENT FLOW IN A CHANNEL FROM A DIRECT SIMULATION

## 1. INTRODUCTION

In this work we present details of the wavenumber - frequency structure of turbulence in a channel obtained from a direct numerical simulation. The work parallels, in certain respects, the experimental findings of Morrison and Kronauer<sup>1</sup>, Morrison et. al<sup>2</sup>, and Bullock et. al<sup>3</sup> in which the detailed structure of the streamwise component of turbulence was investigated in pipe flow. In these experimental investigations, evidence is presented for the existence of a similarity family of waves which extend from the sublayer out into the logarithmic region. Also in that work, a spectral decomposition of the velocity field in the sub-layer revealed an elongated structure whose spanwise length is close to the generally accepted value for the streak spacing observed in flow visualization studies. In addition, wave speeds in the sublayer were found to be several times higher than the local mean velocity.

These experimental findings have shown that a horizontal spectral decomposition of turbulence is remarkably revealing about the nature of turbulent structure. It should be noted, however, that in the experiments cited, only the streamwise component of turbulence was measured. Strictly speaking, however, to test the Morrison-Kronauer wave similarity hypothesis, velocity measurements must be made in the wave system of coordinates. However, as Morrison and Kronauer point out, it is only the wall-normal component of turbulence which remains invariant in wave coordinates so that a strict test of the similarity hypothesis can only be made by determining the structure of this component of the velocity. Experimental difficulties make the determination of the wall-normal component very difficult near the wall. This is one motivation for the determination of the details of the spectral structure of turbulence using a direct numerical simulation.

This work is further motivated by a need for more detailed information on the nature of the sources of wall pressure fluctuations. In Handler, et. al.<sup>4</sup> it was shown that a relatively low resolution calculation exhibits many of the features of the wall

pressure field observed in experiments. However, no details of the turbulent velocity structure which gives rise to the wall pressure structure were given. It is well known, however, that the wall pressure is the result of turbulence interactions throughout the entire flow domain. Specifically, the pressure,  $p(\vec{x}, t)$ , for an incompressible flow is given by the Poisson equation:

$$\nabla^2 p(\vec{x}, t) = \frac{-1}{\rho} \vec{\nabla} \cdot (\vec{\nabla} \cdot \tilde{T}), \quad (1)$$

where  $\rho$  is the density and  $\tilde{T}$ , the Reynolds stress tensor, is given by:

$$\tilde{T} = \hat{e}_\alpha u_\alpha u_\beta \hat{e}_\beta, \quad (2)$$

and  $\vec{u} = u_n \hat{e}_n$  is the velocity. (In the current work, the the subscripts 1, 2, and 3 will designate, for all variables, the streamwise, wall-normal, and spanwise components respectively.) If the velocity is then decomposed into its ensemble averaged component denoted by  $\langle \rangle$ , which for a statistically stationary flow is independent of time, and its fluctuating components, we obtain for the pressure fluctuation,  $p'(\vec{x}, t)$ ,

$$\frac{\nabla^2 p'(\vec{x}, t)}{\rho} = 2 \frac{\partial U_1}{\partial x_2} \frac{\partial u'_2}{\partial x_1} + \partial_\alpha \partial_\beta (u'_\alpha u'_\beta - \langle u'_\alpha u'_\beta \rangle), \quad (3)$$

where primes indicate a turbulent or fluctuating component and  $U_1$  is the mean velocity which is assumed to vary only in the  $x_2$  direction. It has been argued by some (Kraichnan<sup>5</sup>, Meehan and Tavis<sup>6</sup>) that the second term on the right hand side of equation 3, the so called turbulence - turbulence ( $T - T$ ) source, is of secondary importance to the first, the turbulence-mean shear ( $T - M$ ) term. Chase<sup>7</sup> estimates that the ratio of  $T - M$  to  $T - T$  is about 2.5. It is generally accepted, however, that the  $T - M$  source is dominant, though perhaps not throughout the entire wavenumber domain. Since the  $T - M$  term is determined only by the wall-normal component of turbulence,

its structure can be readily computed. This motivates, in part, the direction of the present work.

## 2. COMPUTATIONAL PARAMETERS AND DATA ANALYSIS

The Navier-Stokes equations are solved in rotation form in a channel flow geometry using a pseudo-spectral procedure which is described in Orszag and Kells<sup>8</sup>. In units of the channel half-width,  $h$ , the channel dimensions are  $5 \times 5 \times 2$  in the  $x_1$ ,  $x_3$ , and  $x_2$  directions respectively. The flow is computed at  $64 \times 64$  evenly spaced grid points in the horizontal ( $x_1 - x_3$ ) plane and 65 points, with Chebyshev scaling, are used in the  $x_2$  direction. The initial mean velocity profile is parabolic to which two and three dimensional finite amplitude modes have been added. The Reynolds number ( $R$ ) is 5000 based on  $h$  and  $U_0$ , the initial laminar centerline velocity, and since  $h$  and  $U_0$  are defined as unity,  $R$  is  $1/\nu$ , where  $\nu$  is the kinematic-viscosity. The Reynolds number  $R$  is constant for the duration of the calculation. The Reynolds number  $R^*$  is defined as  $u^*h/\nu$  where  $u^*$  is the friction velocity defined by  $\sqrt{\tau/\rho}$ , and  $\tau$  is the mean shear stress at the wall.

As discussed in detail in Orszag and Patera<sup>9</sup>, the flow will undergo transition to turbulence on a convective time scale. It will then remain in a quasi-stationary state and then decay to some final state on a viscous time scale. The final state is determined by the initial driving force which is fixed in this calculation at  $2/R$ . In the present case, a quasi-stationary state is reached at about  $th/U_0 = 39$ . At this time, data is stored at 512 time steps with a sampling time,  $\Delta t h/U_0$ , of 0.0375. The computational time step duration is 0.00625. During this quasi-stationary period,  $R^*$  varies from 200 to 186 with an average value of about 193.

The principal method used to interpret the data generated in the present calculation is spectral analysis. The reader is referred to [2] for a thorough discussion of the usefulness of employing a Fourier decomposition as opposed to, say, the space-time correlation in facilitating the interpretation of turbulent structure. In the present work,

it is natural to take Fourier transforms of the raw space-time data in the homogeneous ( $x_1 - x_3$ ) plane at selected distances,  $x_2$ , from the wall. The spectral function of interest in the current work,  $\Phi_{ij}$ , is defined by:

$$\Phi_{ij}(\vec{k}, \omega, x_2, x_2') = \frac{1}{L_1 L_3 T} \langle \tilde{U}_i(\vec{k}, \omega, x_2) \tilde{U}_j(\vec{k}, \omega, x_2') \rangle, \quad (4a)$$

and,

$$\frac{1}{(2\pi)^3} \int_{-\infty}^{+\infty} \int_{-\infty}^{+\infty} \int_{-\infty}^{+\infty} \Phi_{ij} dk_1 dk_3 d\omega = u_i u_j, \quad (4b)$$

where  $\tilde{U}_i(\vec{k}, \omega, x_2)$  is the Fourier transform of  $u_i(\vec{x}, t)$ ,  $\vec{k}$  is the wavenumber vector in the horizontal plane,  $\omega$  is the radian frequency,  $L$  is the length (or width of the domain),  $T$  is the run time for one realization, and  $\tilde{U}$  is the complex conjugate of  $U$ . Here, the overbar is defined by equation 9a with an averaging time,  $T_a$ , equal to 9.6 and  $u_i$  represents the velocity with its mean,  $u_i$ , removed.

In the present work the ensemble average is taken over two realizations each of duration  $th/U = 9.6$ . Although this gives a poor estimate of  $\Phi_{ij}$ , the projection spectra defined below have much smaller random errors. We note that the data set is limited in terms of total run time compared to experiments so that if a shorter averaging time was chosen to increase the number of realizations, the low frequencies could not be resolved. A more detailed discussion of the limitations of the calculation is given in §3b.

It is also convenient to non-dimensionalize  $\Phi_{ij}$  using the viscous length,  $l^* = \nu/u^*$ , viscous time,  $t^* = l^{*2}/\nu$ , and square of the variance,  $u_i u_j$ .

$$\Psi_{ij} = \Phi_{ij} (u_i u_j l^{*2} t^*)^{-1}. \quad (5)$$

and

$$\int_{-\infty}^{+\infty} \int_{-\infty}^{+\infty} \int_{-\infty}^{+\infty} \Psi_{ij} dk_1^* dk_3^* d\omega^* = 1, \quad (6)$$

where  $k^* = kl^*$ , and  $\omega^* = \omega t^*$ . The projection spectra are then defined, as in [2], by :

$$\Psi_{ij}(k_1^*, \omega^*) = \int_{-\infty}^{+\infty} \Phi_{ij} dk_3^*, \quad (7a)$$

$$\Psi_{ij}(k_3^*, \omega^*) = \int_{-\infty}^{+\infty} \Phi_{ij} dk_1^*, \quad (7b)$$

$$\Psi_{ij}(k_3^*, k_1^*) = \int_{-\infty}^{+\infty} \Phi_{ij} d\omega^*, \quad (7c)$$

In this work, it is most useful, for reasons given in [1] and [2], to compute the spectra  $\Lambda_{ij}$  defined by:

$$\Lambda_{ij}(k_1^*, \omega^*) = k_1^* \omega^* \Psi_{ij}(k_1^*, \omega^*), \quad (8a)$$

$$\Lambda_{ij}(k_3^*, \omega^*) = k_3^* \omega^* \Psi_{ij}(k_3^*, \omega^*), \quad (8b)$$

$$\Lambda_{ij}(k_1^*, k_3^*) = k_1^* k_3^* \Psi_{ij}(k_1^*, k_3^*), \quad (8c)$$

In these expressions, the dependence on  $x_2^* = x_2/l^*$  and  $x_2^{*l}$  is implied.

### 3. RESULTS

#### A. Stationarity of the Flow and Turbulence Profiles

The scaling arguments given in [9] show that the flow being simulated evolves on a viscous time,  $1/\nu$ . That is, a truly steady state cannot be achieved unless the integration time is very long. However, during transition to turbulence there does exist a quasi-equilibrium between the inner layer and the core of the flow. Classical arguments show that under these conditions a logarithmic layer should exist simultaneously with a well developed inner layer. Though the inner layer develops rapidly, the core continues to evolve slowly. It is during this quasi-equilibrium state that the following results have been obtained.

In figure 1 (a-d) we present the mean velocity profile, and the streamwise, normal, and Reynolds stress intensity profiles. For each plot, there are four curves which are obtained by performing, for a fixed distance above the wall, an average over the horizontal plane and a temporal average over one quarter of the total time used in the analysis. This averaging procedure is represented by:

$$u(x_2, t_0) = \frac{1}{T_a} \int_{t_0}^{t_0+T_a} \langle u(\vec{x}, t) \rangle_h dt, \quad (9a)$$

$$\langle u(\vec{x}, t) \rangle_h = \frac{1}{L_1 L_3} \int_0^{L_1} \int_0^{L_3} u(\vec{x}, t) dx_1 dx_3, \quad (9b)$$

where the averaging time,  $T_a$ , is 4.8 and each curve is distinguished by  $t_0$  which has values 39.2, 44.0, 48.8 and 53.6 as indicated in figure 1. Also, the data in each time interval is scaled by the average  $u^*$  for that time interval.

The mean velocity profiles (fig. 1-a) show a well developed sublayer in the region  $0.23 \leq x_2^* \leq 3.7$ . A logarithmic region exists for  $65 \leq x_2^* \leq 150$ . The flow in this region is only quasi-stationary as indicated by the slow decrease in the mean velocity with time. However, to a good approximation, the expression  $u_1/u^* = .415^{-1} \ln x_2^* + 6.8$ , describes the mean velocity profile in this region.

The streamwise and wall-normal turbulence intensity profiles are shown in figures 1-b and 1-c. These results may be compared with those of Kreplin and Eckelmann<sup>10</sup> who made measurements in a channel with a Reynolds number based on half-width and centerline velocity of 3850 compared with the somewhat lower value of 3680 in the present study. The comparison is good for  $u_1^{rms}/u^*$  for  $x_2^* \leq 5$  and for  $u_2^{rms}/u^*$  for  $x_2^* \leq 40$ . The root-mean-square value of a fluctuating quantity,  $f^{rms}$ , is defined here as  $f^{rms} = \sqrt{\overline{f^2}}$ . The experimental results indicate a peak value for  $u_1^{rms}/u^*$  of 2.85 at  $x_2^* \simeq 13$  and a peak for  $u_2^{rms}/u^*$  of 1.0 at  $x_2^* = 40$ . The calculations show peak values for  $u_1^{rms}/u^*$  ranging from 3.04 to 2.28 at  $x_2^* \simeq 65$  and peak values for  $u_2^{rms}/u^*$  ranging from 1.91 to 1.28, which occurs at or near the centerline. In figure 1-d, the  $\overline{u_1 u_2}/u^{*2}$  profiles are in good agreement in the core region with the asymptotic ( $R^* \rightarrow \infty$ ) limit for the second half of the calculation but the stresses are too high early in the run.

These disagreements between experiment and calculation are due primarily to two factors. The first is the relatively short duration of the quasi-stationary turbulence. During this time the outer regions of the flow are not well developed. This problem can only be remedied by computing much further out in time. This has been done in a recent higher resolution direct calculation<sup>13</sup> which also starts with laminar initial conditions. In that calculation, a constant driving force is chosen so that the steady state wall shear stress achieves a value significantly higher than the initial laminar value. At the end of the calculation the peak in  $u_1^{rms}/u^*$  occurs at  $x_2^* \simeq 23$ . The run time of the higher resolution calculation will be significantly increased to see if convergence with experiment is obtained. We also note that in [11] it is shown that the incorporation of subgrid scale models obtained from a renormalization group analysis gives turbulence peaks much closer to the wall in a relatively short time starting from laminar initial conditions.

The second source of disagreement is the lack of good spanwise resolution. Orszag, et. al.<sup>11</sup> have shown that good spanwise resolution is crucial and this is due to the necessity of capturing the near wall dynamics of the bursting process. Recent results

of Leighton<sup>12</sup>, however, using the identical data set used in obtaining the results of this paper, show that the bursting process is at least nominally captured by the current spanwise resolution of about 15 viscous units. With these qualifications in mind, the structure of the turbulent field will now be described.

## B. Visual Observations and Spectra

Certain structural features of the streamwise and wall normal velocity fields can be determined, at least qualitatively, by viewing contour plots of the velocity in horizontal planes at a fixed instant in time. In figures 2(a-d) and 3(a-d) we have exhibited such plots for the  $u_1$  and  $u_2$  fields, respectively. For the  $u_1$  component, we plot the contours  $(u_1 - \langle u_1 \rangle_h) - u_1^{rms}$  and  $(u_1 - \langle u_1 \rangle_h) - (0.25 \times u_1^{rms})$  and for  $u_2$  we plot the contours  $u_2 + u_2^{rms}$  and  $u_2 + (0.25) \times u_2^{rms}$ . That is, the streamwise velocity contours correspond to fluctuations in the opposite direction to the mean flow and the wall-normal velocity contours represent fluctuations away from the wall. These contour levels are chosen to correspond to low speed regions of the flow which, near the wall, are normally observed in flow visualization studies as streaks. In effect, two such plots, one of  $u_1$  and one of  $u_2$  at same elevation above the wall, will give instantaneous contours of second quadrant Reynolds stresses.

In figure 2-a, ( $x_2^+ = 2.11$ ) we note that the  $u_1$  velocity structure is clearly elongated in the flow direction. The corresponding plot of  $u_2$  in figure 3-a also shows an elongated structure and is very strongly correlated with the corresponding  $u_1$  structure. However, the normal velocity structure is distinctly different from the streamwise structure in that the  $u_2$  contours are not strongly elongated in the flow direction and appear to be distinctly finer grained. At  $x_2^+ = 27.7$ , we observe a  $u_1$  structure at a spanwise location of about 3.5 that extends the entire length of the flow domain. No such structure is clearly evident in the  $u_2$  field. At  $x_2^+ = 94.75$ , the edge of the logarithmic layer, only  $u_1$  structures of spanwise wavelength on the order of the box dimensions exist whereas

in the corresponding  $u_2$  plot the structures are not nearly as large. We also note a lack of any significant correlation between  $u_1$  and  $u_2$  at this level above the wall.

Before discussing the spectral structure of these fields, it is appropriate at this point to indicate the limitations of the present calculations, in addition to the problems associated with non-stationarity and the early state of development of the turbulence discussed earlier. These constraints are those imposed by the computational domain size and grid spacing, which determine the lowest and highest resolvable wavenumbers, and total computational time and time step size, which determine the lowest and highest resolvable frequencies. In the current calculation, the grid resolution in the horizontal plane is about 15.2 in viscous units and the horizontal plane is about  $975 \times 975$  in these same units. These dimensions give 0.0064 and 0.205 for the lowest and highest wavenumbers,  $k^*$ , respectively. Similarly, the total run time in viscous units is 146 and the sampling time is 0.285. This gives 0.043 and 11.0 for the lowest and highest radian frequencies,  $\omega^*$ , respectively.

However, these limits on the range of the data in wavenumber-frequency coordinates were modified because of computer memory limitations in the process of computing spectra from the raw data. These limits, again in viscous units, are .00644 and 0.0966 for the lowest and highest streamwise and spanwise wavenumbers and 0.0861 and 11.0 for the lowest and highest radian frequencies. The analysis is therefore confined to approximately a one order of magnitude variation in wavenumber and two orders of magnitude in frequency. We also note that spanwise structures with wavelengths,  $\lambda^*$ , on the order of 100, the so called sublayer streak spacing, are expected to appear at  $k_3^* = 0.063$  so that such information is within (though admittedly at the very high end) of the calculated spectra. We also observe that in experiments<sup>1,2,3</sup>, at least a two order of magnitude range was covered in  $k^* - \omega^*$  coordinates. This allows a resolution of not only the small structures near the wall but large structures observed in the logarithmic portion of the velocity profile. In this region, significant structure is observed for radian frequencies below  $10^{-2}$ . It is clearly not possible to investigate

this region of the spectrum in the present study. However, certain qualitative behavior of the spectral structure can be discerned.

With these limitations in mind, examples of the projection spectra,  $\Lambda_{11}$  and  $\Lambda_{22}$ , are shown in figures 4 (a-1) and 5 (a-d) respectively. In these plots the spectra displayed are those for which  $x_2^* = x_2^{*'}$ . In the sublayer, at  $x_2^* = 5.84$ , the  $u_1$  field exhibits a definite peak in the  $k_1^* - \omega^*$  spectrum, but the convective ridge is not well defined. The  $k_1^* - k_3^*$  spectrum exhibits a well defined peak at  $k_3^* \simeq 0.09$  and  $k_1^* \simeq 0.026$ . These values correspond to a spanwise wavelength of 69.7 and a streamwise wavelength of 243, indicating structures which are clearly elongated. It would be tempting to state at this point that this peak in spectrum corresponds to the streaky structure observed experimentally by many investigators. The spanwise wavelength of 69.7, however, is considerably smaller than the generally accepted value of about 100. Morrison and Kronauer<sup>2</sup> obtained  $\lambda_3^* = 135$  in their experiment using the same spectral analysis. On the other hand, some investigators have found values for  $\lambda_3^*$  less than 100, notably the measurement of Runstadler<sup>14</sup>. Though we cannot draw a definite conclusion as to the origin of this peak at the present time, it is encouraging that the  $k_1^* - k_3^*$  spectrum corresponds to the visual evidence of an elongated structure shown in the contour plots. More detailed analysis of higher resolution data is currently in progress to determine more clearly the origin of this peak.

At  $x_2^* = 27.7$  we see that the  $k_1^* - \omega^*$  spectrum of the streamwise velocity component has a clearly defined convective ridge. It is also clear from the  $k_1^* - k_3^*$  spectrum, that the fluctuation energy begins to shift to lower wavenumbers at this distance from the wall. At  $x_2^* = 64$ , the bottom edge of the logarithmic layer, this shift is evident. A spectral peak is clearly defined in the  $k_3^* - \omega^*$  spectrum at  $k_3^* = 0.028$  or  $\lambda_3^* = 223$ . There is a further spectral shift at  $x_2^* = 166.4$ , the outer part of the logarithmic layer, to about  $k_3^* = 0.019$  or  $\lambda_3^* = 331$ . This wavelength corresponds roughly to that of the width of the channel,  $2h$ . A transition from length scales on the order of the streak

spacing to that of the channel width seems to occur smoothly as we move across the buffer layer.

This transition of length scales is also clearly evident in the transition of the local convection velocities as shown in figure 6. In this figure we have computed the convection velocity of the streamwise fluctuations at several locations above the wall by selecting, at various wavenumbers, the frequency which corresponds to the maximum in the  $k_1^* - \omega^*$  spectrum. An estimate of the convection velocity can then be made using the average value of  $c^* = k_1^*/\omega^*$  at several locations along the convective ridge. In figure 6, we plot  $c^*$ , (the convection velocity,  $c$ , normalized with  $u^*$ ) and the ratio  $c/\langle u_1 \rangle$  where  $\langle u_1 \rangle$  is the local streamwise velocity which is obtained by averaging both horizontally and over the total time of the run. The local convection velocity is clearly much larger than the local mean speed in the sublayer. This is not inconsistent with experimental results [2] which indicate that the convection velocities normalized with the local mean velocity vary from about 5 at  $x_2^* = 1.52$  to 2 at  $x_2^* = 5.93$ . The values obtained here are somewhat higher, ranging from 6.8 at  $x_2^* = 2.1$  to 2.7 at  $x_2^* = 5.04$ . The calculations also show that the convection velocities in the sublayer are remarkably constant at about  $c^* = 14$ . This is higher than the experimental result of [2] in which  $c^*$  is found to be about 8.0, but the experiments also show that this speed is unchanged throughout the sublayer. For  $x_2^* \geq 10$ , the calculation shows that  $c^*$  gradually increases to about 19 in the logarithmic layer which is only slightly above the local mean flow velocity. All of these results are consistent, at least qualitatively, with the experimental results though it is not possible on the basis of the current computational evidence to confirm or reject the hypothesis proposed in [2] that such high speeds in the sublayer are in fact due to a wave phenomenon.

Representative spectra for the  $u_2$  fluctuations shown in figure 5 are different in some respects from the  $u_1$  spectra. This should certainly be expected from the obvious differences shown in the contour plots. The most notable difference is the absence of an energy peak at wavelengths corresponding to the sublayer streak spacing. The  $k_1 - k_3$

spectrum for  $x_2^* = 11.4$  indicates a possible peak at a  $k_3^*$  coordinate much higher than that found the  $u_1$  field. Also, at  $x_2^* = 64$ , the edge of the logarithmic layer, the  $u_2$  energy begins to shift noticeably toward large length scales. The energy has clearly shifted to scales on order of the channel size at  $x_2^* = 166.3$ . It therefore appears that the  $u_2$  field has generally a smaller structure than  $u_1$  and this is completely consistent with visual observation. The author, however, is not aware of any experimental data on the wall normal velocity which can be used for comparison.

### C. Structure of the Wall Pressure Field

As discussed in [15] and [16], we may expect, from theoretical considerations, certain differences between the structure of the wall pressure field in a channel flow and its structure in a boundary layer flow. In particular, in strictly incompressible flow we expect the spectral density of the pressure field to vanish as the wavenumber approaches zero. This does not appear to be the case in a channel flow. Nevertheless, we should not expect significant differences in the overall structure of the wall pressure field.

In figure 7 (a-c), we show the space-time correlations of the pressure field obtained in the present calculation. These correlations are defined by:

$$R_{pp}(\Delta x_1^*, \Delta t^*) = \int_{-\infty}^{\infty} \int_{-\infty}^{\infty} \Psi_{pp}(k_1^*, \omega^*) e^{j(k_1^* \Delta x_1^* - \omega^* \Delta t^*)} dk_1^* d\omega^*, \quad (10a)$$

$$R_{pp}(\Delta x_3^*, \Delta t^*) = \int_{-\infty}^{\infty} \int_{-\infty}^{\infty} \Psi_{pp}(k_3^*, \omega^*) e^{j(k_3^* \Delta x_3^* - \omega^* \Delta t^*)} dk_3^* d\omega^*, \quad (10b)$$

$$R_{pp}(\Delta x_3^*, \Delta x_1^*) = \int_{-\infty}^{\infty} \int_{-\infty}^{\infty} \Psi_{pp}(k_3^*, k_1^*) e^{j(k_3^* \Delta x_3^* + k_1^* \Delta x_1^*)} dk_3^* dk_1^*, \quad (10c)$$

In these expressions, the spectrum of the wall pressure,  $\Psi_{pp}$ , is defined in an analogous fashion to the spectrum of the velocity field,  $\Psi_{ij}$ , given in equation 7. It

is convenient to examine the pressure field in space-time coordinates (rather than in transform space) for present purposes simply because in these coordinates the gross behavior of the results are more easily interpreted and compared with the available experimental results. (In [16] the pressure field structure is given in spectral coordinates and the ratio of the root mean square pressure to the wall shear stress is found to be 3.915.) The function  $R_{pp}(\Delta x_1^*, \Delta t^*)$  shows a clearly defined convective ridge. A line showing the approximate position of this ridge shows clearly that the convection velocity,  $c^* = d\Delta x^*/d\Delta t^*$ , (that is the slope of the line defining this ridge), is not constant. The convection velocity at very small streamwise spatial separations is about 12.1 and at very large separations (say  $\Delta x_1^* \geq 300$ ) it is about 13.4. The ratios of these velocities to the centerline velocity are 0.64 at small separations and 0.70 at large separations. These results are certainly in qualitative agreement with the results of Blake<sup>17</sup>, Bull<sup>18</sup>, and Willmarth<sup>19</sup>. It is also consistent with the idea that since the pressure field is driven by sources that exist throughout the flow domain, one expects smaller convection speeds at small separations (say, separations that are at least an order of magnitude smaller than the largest scales of the flow) since this region of the space-time correlation may be more representative of structures whose centers are close to the wall where local convection speeds are small.

Also, from elementary theoretical considerations we must expect that if the turbulence-mean shear source term is dominant, that the factor  $k_1/|k| = \cos\theta$ , where  $k = |\vec{k}|$  and  $\theta$  is the angle between  $\vec{k}$  and the flow direction, will dominate the spectral characteristics. This structure is indeed observed in the experiments of Bull<sup>17</sup> who measured  $R_{pp}(\Delta x_1^*, \Delta x_3^*)$ . For a constant correlation value of 0.1 he obtained a contour whose elongation in the spanwise direction was about 2.7 times that in the streamwise direction. The present calculations give a ratio of about 3.3. In addition, we note that the calculations give approximately concentric correlation contours for  $R_{pp}(\Delta x_1^*, \Delta x_3^*)$  at small separations indicating a nearly isotropic small scale field. This is also in excellent agreement with experimental results. Finally, the  $R_{pp}(\Delta x_3^*, \Delta t^*)$  contours show no

indication of spanwise convection and are almost perfectly symmetric about  $\Delta t^* = 0$ . In general, the qualitative agreement between these wall-pressure results and available experiments is excellent, but the nature of the sources of the pressure field can only be obtained by computing the dependence of the velocity correlations on the wall-normal coordinate. To this end, preliminary results on the wall-normal structure of  $u_2$  have been computed and are presented next.

#### D. Wall-normal Structure of the Vertical Component of Velocity

As indicated in the introduction, the structure of the  $u_2$  velocity component determines the structure of the T-M source of the wall pressure field. As a preliminary indication of this structure, we compute both the broadband correlation coefficient,  $\beta_{22}$ , and the correlation coefficient in narrow frequency bands,  $\alpha_{22}$ . These functions are defined by:

$$\phi_{22}(x_2, x'_2) = \int_{-\infty}^{+\infty} \int_{-\infty}^{+\infty} \Phi_{22}(\vec{k}, \omega, x_2, x'_2) d\vec{k} d\omega, \quad (11a)$$

$$\beta_{22}(x_2, x'_2) = \frac{\phi_{22}(x_2, x'_2)}{\sqrt{\phi_{22}(x_2, x_2)\phi_{22}(x'_2, x'_2)}}, \quad (11b)$$

$$\phi_{22}(\omega, x_2, x'_2) = \int_{-\infty}^{+\infty} \Phi_{22}(\vec{k}, \omega, x_2, x'_2) d\vec{k}, \quad (11c)$$

$$\alpha_{22}(\omega, x_2, x'_2) = \frac{|\phi_{22}(\omega, x_2, x'_2)|}{\sqrt{\phi_{22}(\omega, x_2, x_2)\phi_{22}(\omega, x'_2, x'_2)}}, \quad (11d)$$

where  $\Phi_{22}$  is defined by equation (4). We also compute the phase difference,  $\theta$ , given by:

$$\theta(\omega, x_2, x'_2) = \tan^{-1} \frac{\text{Im}(\phi_{22}(\omega, x_2, x'_2))}{\text{Re}(\phi_{22}(\omega, x_2, x'_2))}. \quad (12)$$

In figure (8a) we plot  $\beta_{22}(x_2, x_2')$ . For each curve,  $x_2'$  is fixed at 11.4, 64.03, 129.31, and 166.39 in viscous units and  $x_2$  is varied. The asymmetry of  $\beta_{22}$  is clear. That is, for each curve, the rate of decay of the correlation coefficient is larger for  $x_2 < x_2'$ . We also note that  $\beta_{22}$  is positive across the entire width of the channel. These two characteristics are qualitatively consistent with the experimental measurements of Comte-Bellot<sup>20</sup>. For clarity at smaller separations, this same data is shown on a semi-log plot in figure 8(b). In figure 8(c), the same data is plotted against  $x_2/x_2'^{ref}$ , where  $x_2'^{ref}$  is the fixed reference coordinate for each plot. It is clear that the broadband correlations cannot be forced to collapse over the entire width of the channel although there appears to be a limited region of collapse for  $x_2'^{ref} = 64.03, 129.31$  and  $166.39$  for  $x_2/x_2'^{ref} \leq 1$ .

The wave similarity hypothesis proposed in [1] and [2], however, suggests that  $\omega$  may be used to constrain  $|\vec{k}|$ , at least approximately. This led Bullock, et. al.[3] to propose that  $\alpha_{22}$  could be reduced to a dependence on only two parameters,  $x_2/x_2'^{ref}$ , and  $\omega x_2'^{ref}$ . With this as motivation we plot, in figure 9(a-c),  $\alpha_{22}$  for three values of  $\omega x_2'^{ref}$ , though the value of this parameter could not be held absolutely constant because of the discrete nature of the data. The collapse is not nearly as good as the experimental data given in [3] but part of the reason for this can clearly be attributed to the lack of sufficient data needed to reduce statistical scatter in the spectral estimates. However, it is clear from these plots that the correlation length is decreasing with increasing  $\omega x_2'^{ref}$  which is consistent with the experimental results given in [3]. In figure [10] we plot the phase change,  $\theta$ , given by equation 12, against  $x_2$  for  $x_2'^{ref} = 64.05$  for four different frequencies. This again shows a typical asymmetry with respect to the side of the channel above and below the fixed reference point. We also note larger phase differences for larger frequencies. These results are also qualitatively consistent with the results of [3], though in that work only the streamwise component of turbulence was measured.

#### 4. SUMMARY AND CONCLUSIONS

The wavenumber-frequency structure of a quasistationary turbulent flow has been computed from data generated from a direct simulation in a channel. Although the turbulence is in an early stage of development, certain features of the velocity structure compare favorably with experimental results. In particular, the spanwise periodicity of the streamwise velocity component in the sublayer is clearly evident in contour plots of the field and in the corresponding  $k_1 - k_3$  spectrum which indicates a spanwise wavelength of 69.7 (in viscous units) for this structure. The local wave speeds computed from the  $k_1 - \omega$  spectrum of the streamwise velocity component are as much as 6.8 times the local average streamwise velocity in the sublayer. The ratio of the wave speed to the local mean speed decreases across the buffer layer and is approximately equal to one in the logarithmic layer. Also, the ratio of the wave speed to friction velocity remains constant at about 14 throughout the sublayer. In general, these results are consistent with the experimental results described in [1] and [2]. The spectra and contour plots for the wall-normal component of velocity indicate a structure which is more finely grained than that of the streamwise velocity component. Additionally, the wall-normal component lacks a clearly defined periodic spanwise structure in the sublayer.

The space-time correlations of the wall-pressure field reveal features which are remarkably close to experimental observations. First, wave speeds at small separations are somewhat lower than speeds at large separations, which is consistent with most experimental results. Secondly, the spanwise-streamwise correlations reveal an isotropic structure at small separations and highly anisotropic structure at large separations. At larger separations the spanwise length scale is about 3 times the streamwise scale. This is consistent with experiments as well as with elementary theoretical considerations. Also, the wall-normal structure of  $u_2$ , which determines the structure of the turbulence-mean shear source of wall pressure, is computed. An asymmetry exists in the broadband correlation coefficient with respect to the fixed location,  $x_2''^J$ . Following the conjecture postulated in [3], the correlation coefficients computed in narrow frequency bands are plotted against  $x_2/x_2''^J$  with  $\omega x_2''^J$  fixed. A fair collapse of the

data is obtained with a more rapid decay of the correlation for higher values of  $\omega r_2^{r'f}$ . The statistical scatter in these narrow band correlations is considerable.

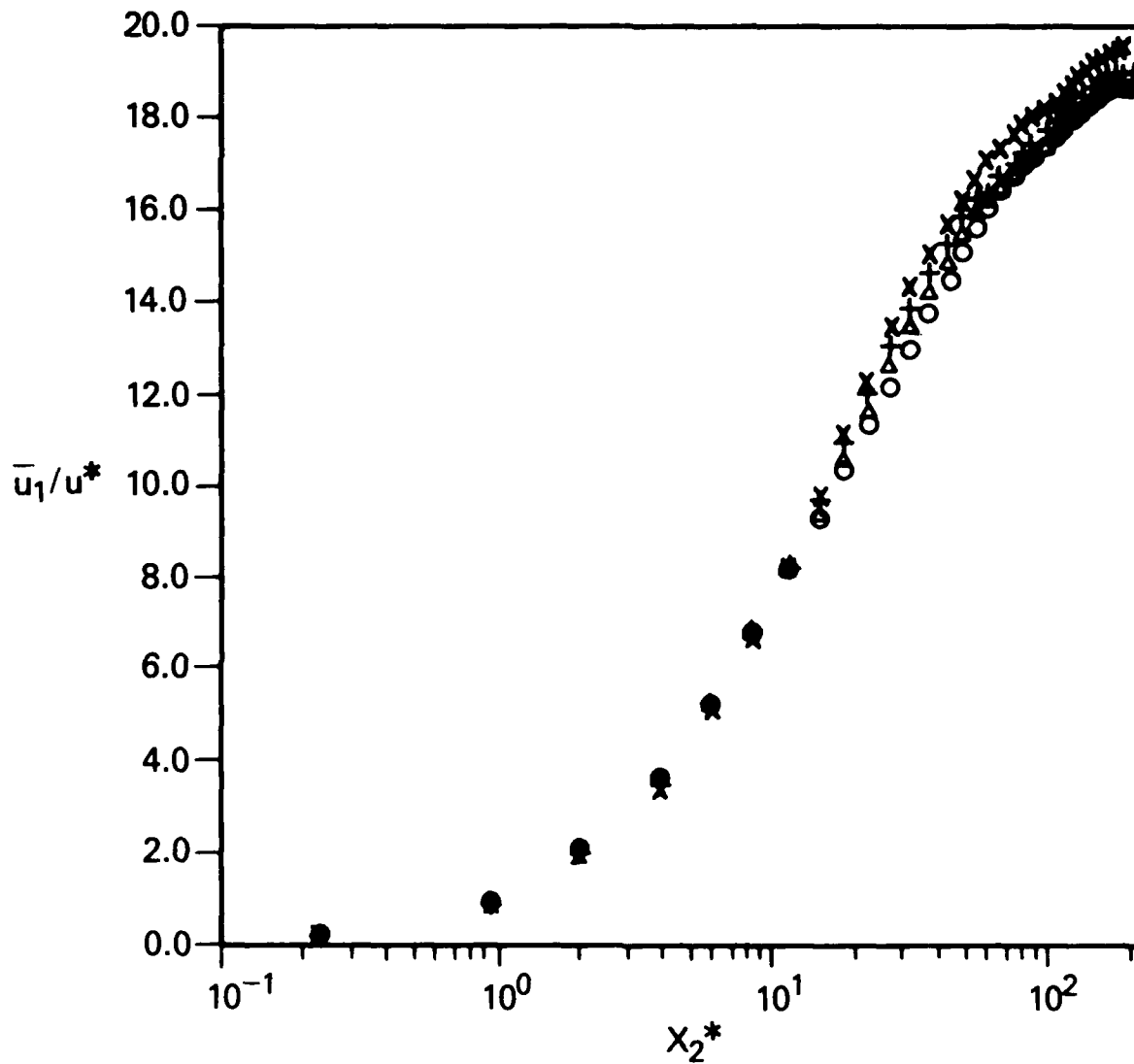
Although several aspects of this work, including a nonstationary turbulence and the limited range of the results at low frequencies and wavenumbers, limit its usefulness in terms of comparison with the details of experiments, the results are close enough to experiments to warrant the use of direct simulation data to elucidate the nature of the sources of the wall pressure field. In particular, data obtained from higher resolution direct simulations will be used in the future to study the detailed structure of both the turbulence- mean shear and turbulence - turbulence sources of the wall pressure field and relevant pressure-velocity correlations.

### ACKNOWLEDGMENTS

This work was supported by the Office of Naval Research and the Naval Research Laboratory. The author also wishes to thank Dr. Richard I. Leighton for many useful discussions and Mr. Daniel M. Carroll for his assistance with the graphics.

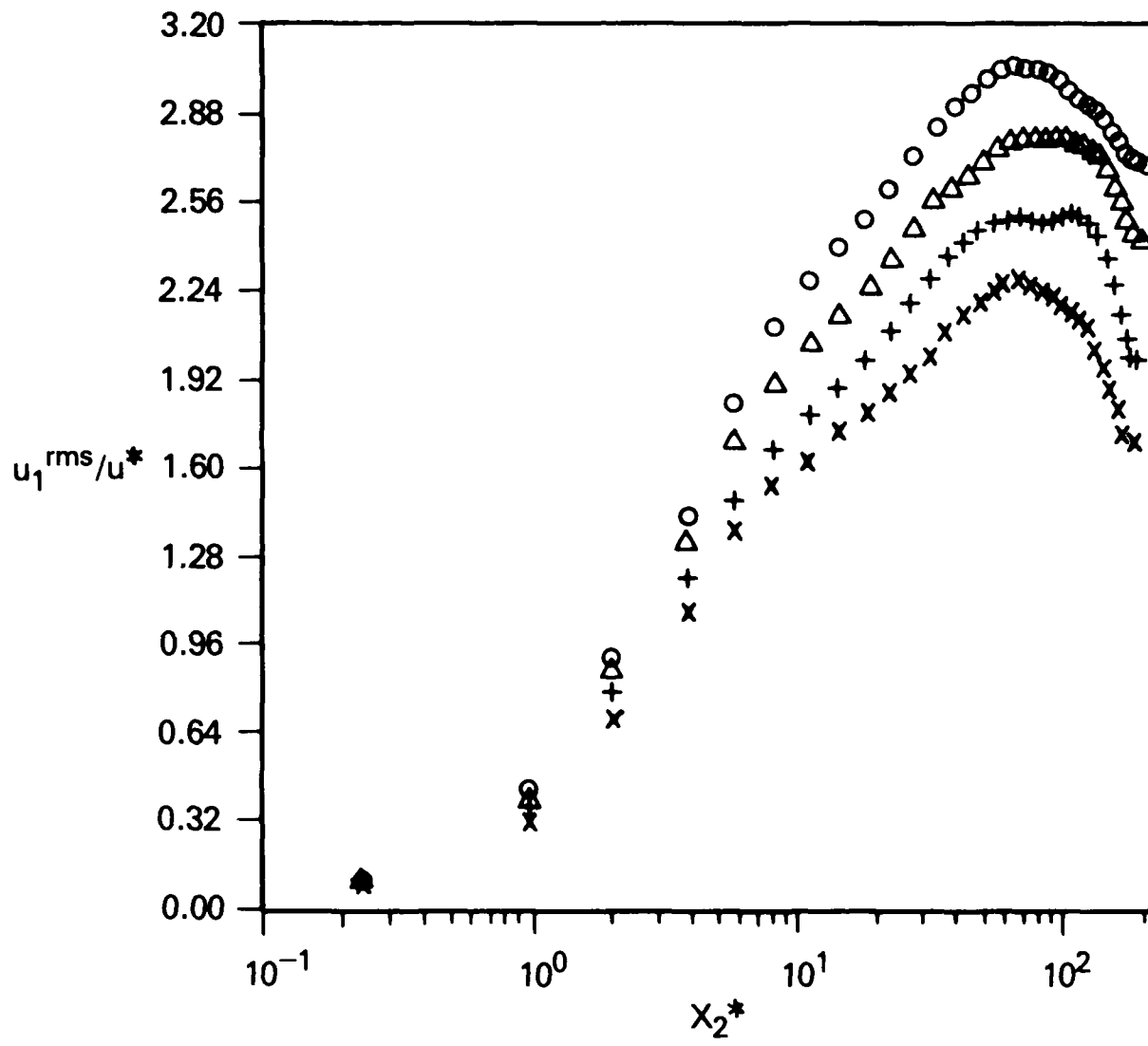
## REFERENCES

1. W.R.B. Morrison and R.E. Kronauer, *J. Fluid Mech.*, **39**, pp.117-141, (1969).
2. W.R.B. Morrison, K.J. Bullock, and R.E. Kronauer, *J. Fluid Mech.*, **47**, pp. 639-656, (1971).
3. K.J. Bullock, R.E. Cooper, and F.H. Abernathy, *J. Fluid Mech.*, **88**, pp.585-608, (1978).
4. R.A. Handler, R.J. Hansen, L. Sakell, S.A. Orszag, and E. Bullister, *Phys. of Fluids*, **27**, pp.579-582, (1984).
5. R.H. Kraichnan, *Phys. of Fluids*, **28**, 378-390, (1956).
6. W.C. Meecham and M.T. Tavis, *Phys. of Fluids*, **23**, pp.1119-1131, (1980).
7. D.M. Chase, *J. Sound Vib.*, **70**, pp. 29-67, (1980).
8. S.A. Orszag and L.C. Kells, *J. Fluid Mech.*, **96**, pp.159-205, (1980).
9. S.A. Orszag and A.T. Patera, *Phys. Rev. Lett.*, **47**, pp.832-835, (1981).
10. H. P. Kreplin and H. Eckelman, *Phys. of Fluids*, **22**, pp.1233-1239, (1979).
11. S.A. Orszag, V. Yakhot, and A. Yakhot, Fifth International Beer-Sheva Seminar on MHD Flows and Turbulence (March 1987).
12. R.I. Leighton, Ph.D. Thesis, University of Michigan, (1986).
13. R.A. Handler, R.I. Leighton, D.M. Carroll, "High Resolution Simulation of Turbulence in a Channel", Naval Research Laboratory Memorandum Report, in preparation, (1987).
14. P. W. Runstadler, S.J. Kline, and W.C. Reynolds, Mech. Eng. Dept. Rept. MD-8, Stanford University, (1963).
15. R.A. Handler, R.J. Hansen, R. Leighton, and S. Orszag, IUTAM Symposium on Aero- and Hydro-Acoustics, Lyon, France, pp.261-268, (1985).
16. R. J. Hansen, R. A. Handler, R.I. Leighton, and S.A. Orszag, *J. Fluids and Structures*, to appear (October, 1987).
17. W.K. Blake, *J. Fluid Mech.*, **44**, pp.637, (1970).
18. M.K. Bull, *J. Fluid Mech.*, **28**, 719-754, (1967).
19. W.W. Willmarth and C.E. Woolridge, *J. Fluid Mech.*, **14**, 187, (1962).
20. G. Comte-Bellot, Publications Scientifiques et Techniques du Ministere de l'Air, (1965).



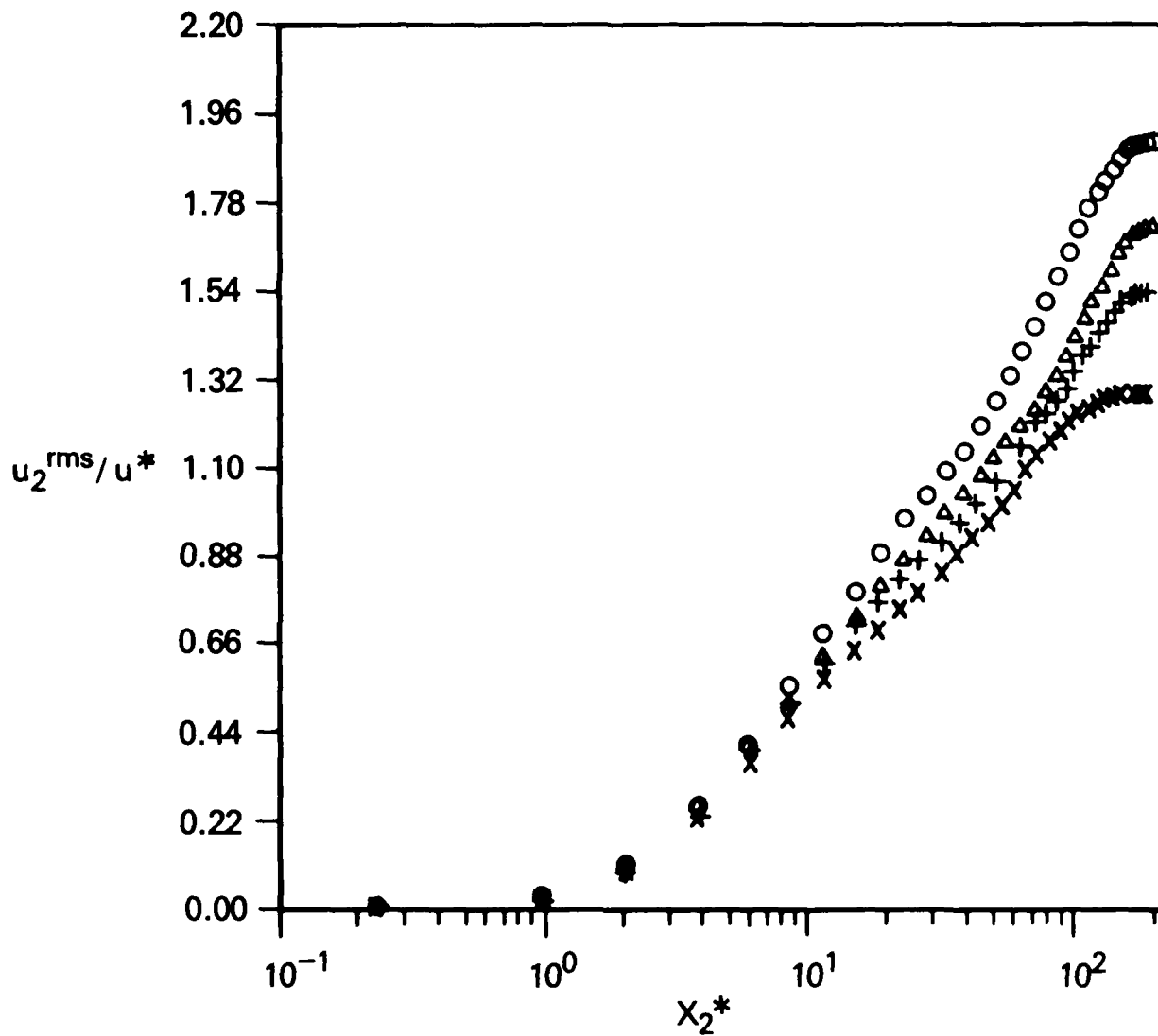
(a) streamwise velocity

Fig. 1 — Global turbulence properties obtained from the averaging defined by equation 9. Curves are distinguished by the lower limits of the time integration given by:  $\circ$ ,  $t_0 = 39.2$ ,  $\Delta$ ,  $t_0 = 44.0$ ,  $+$ ,  $t_0 = 48.8$ ,  $\times$ ,  $t_0 = 53.6$ .



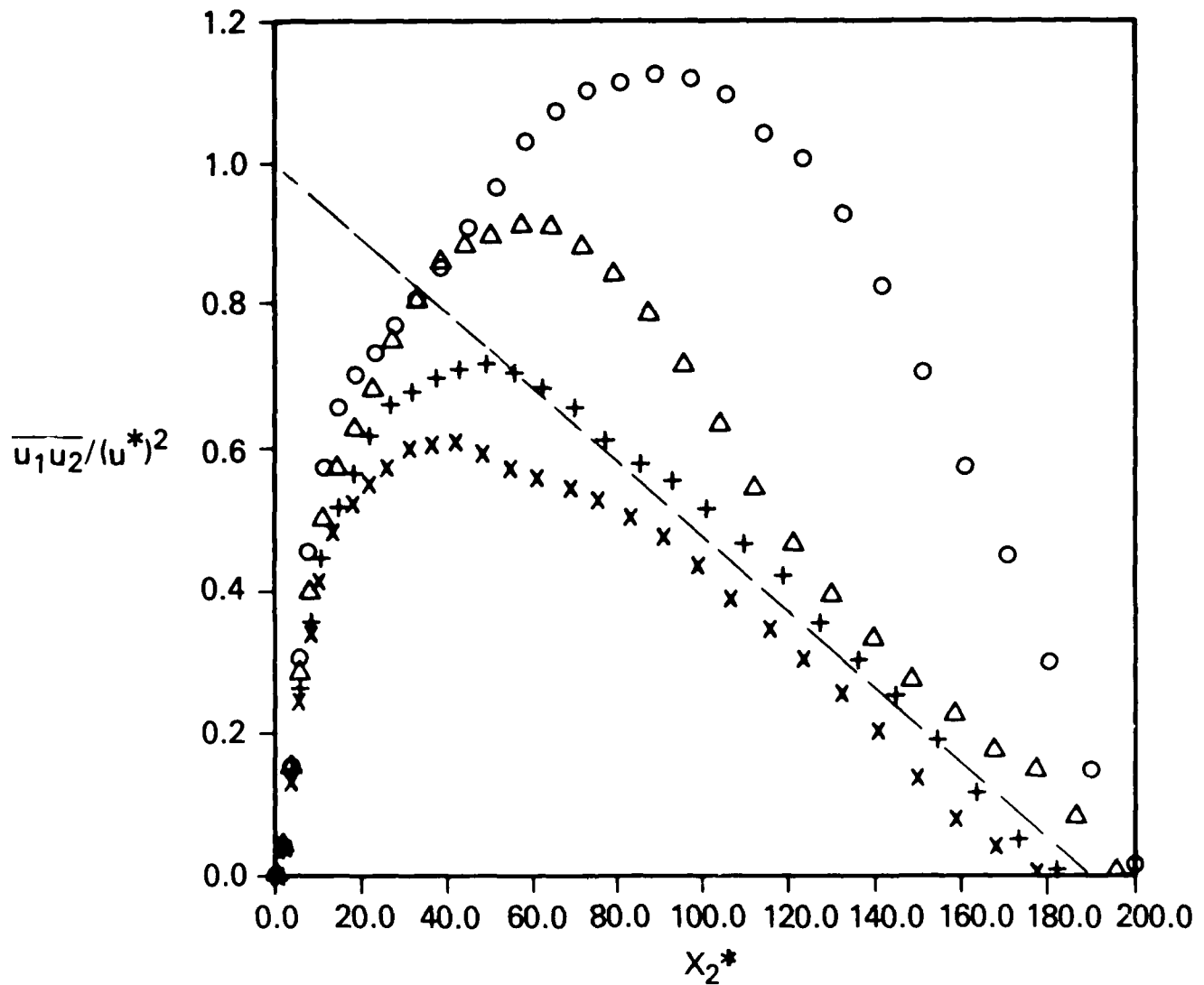
(b) root mean square streamwise velocity

Fig. 1 — (Continued) Global turbulence properties obtained from the averaging defined by equation 9. Curves are distinguished by the lower limits of the time integration given by:  $\circ$ ,  $t_0 = 39.2$ ;  $\Delta$ ,  $t_0 = 44.0$ ;  $+$ ,  $t_0 = 48.8$ ;  $\times$ ,  $t_0 = 53.6$ .



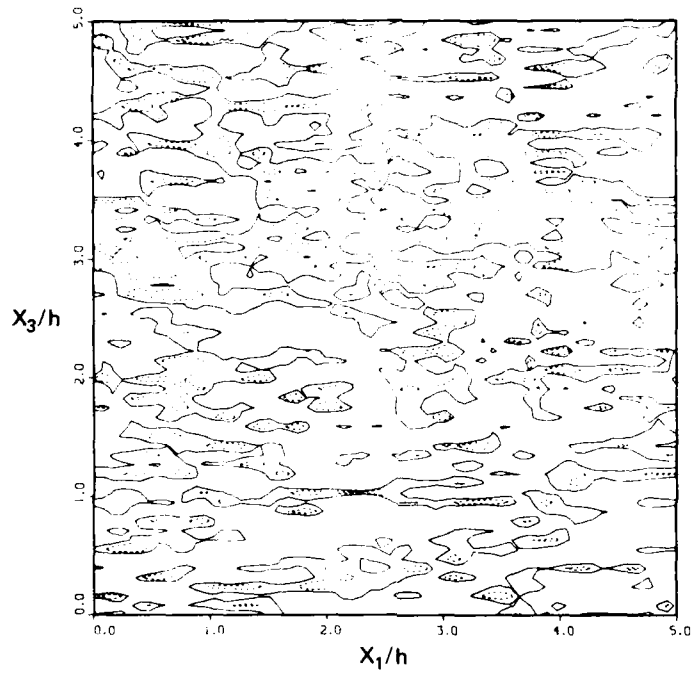
(c) root mean square wall normal velocity

Fig. 1 — (Continued) Global turbulence properties obtained from the averaging defined by equation 9. Curves are distinguished by the lower limits of the time integration given by:  $\circ$ ,  $t_0 = 39.2$ ;  $\Delta$ ,  $t_0 = 44.0$ ;  $+$ ,  $t_0 = 48.8$ ;  $\times$ ,  $t_0 = 53.6$ .

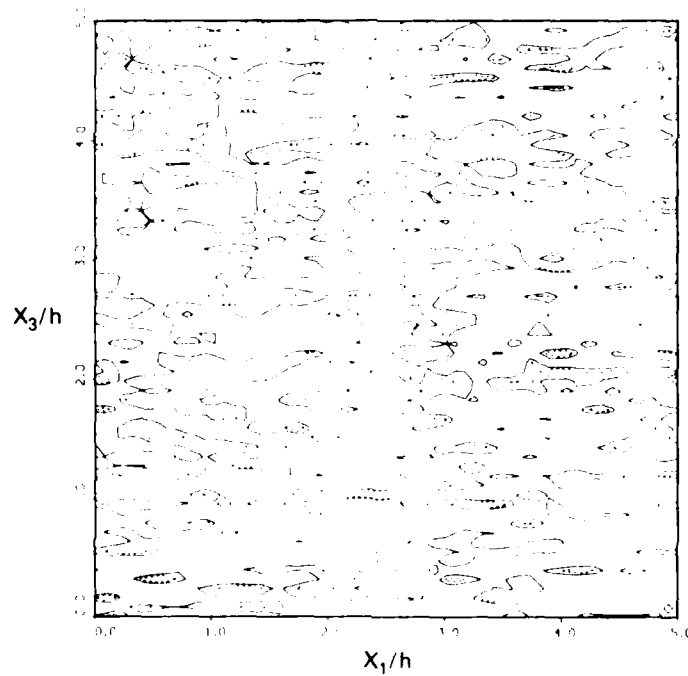


(d) Reynolds stress: - - -, asymptotic ( $R^* \rightarrow \infty$ ) limit for Reynolds stress.

Fig. 1 - (Continued) Global turbulence properties obtained from the averaging defined by equation 9. Curves are distinguished by the lower limits of the time integration given by:  $\circ, t_0 = 39.2$ ,  $\Delta, t_0 = 44.0$ ,  $+, t_0 = 48.8$ ,  $\times, t_0 = 53.6$ .

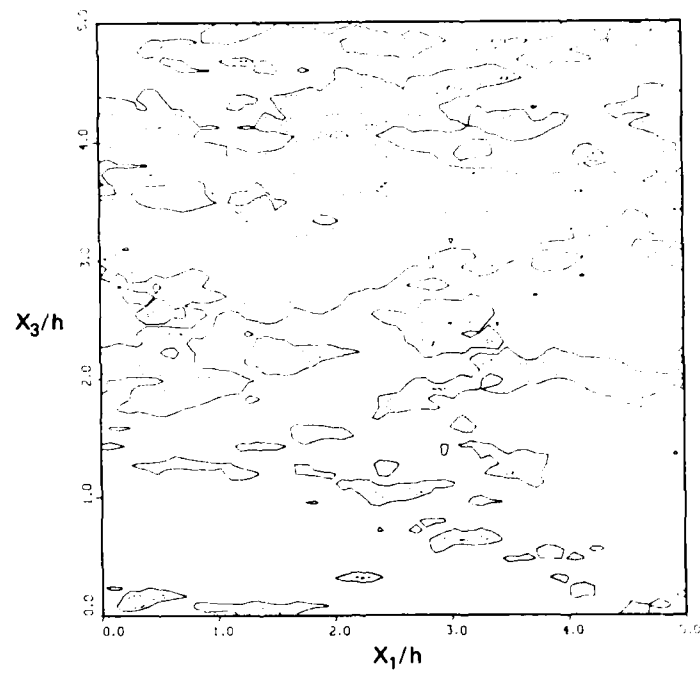


(a)  $x_2^* = 2.11$

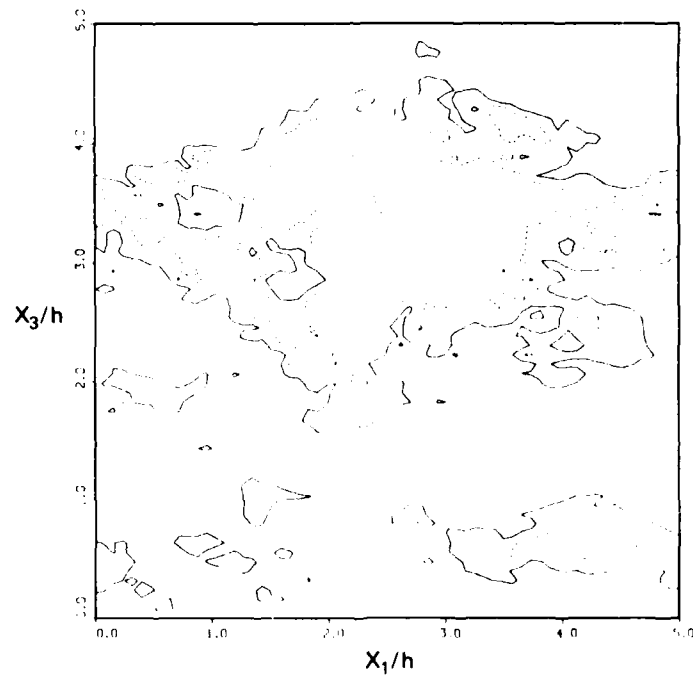


(b)  $x_2^* = 5.84$

Fig. 2 — Contours of constant streamwise velocity. Contour levels are given by: — — —  $(u_1 - \langle u_1 \rangle_h) - u_1^{rms}$ , — — —  $(u_1 - \langle u_1 \rangle_h) - (.25 \times u_1^{rms})$ .

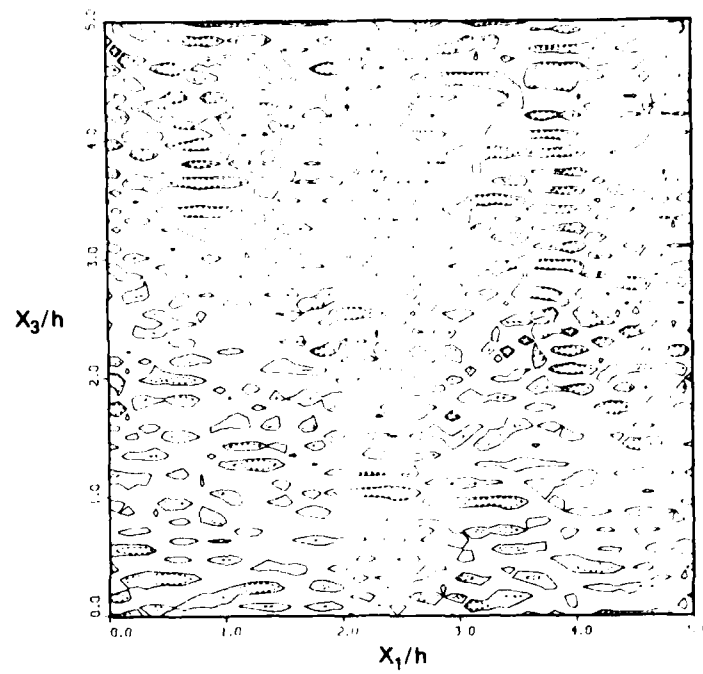


(c)  $x_2^* = 27.74$ .

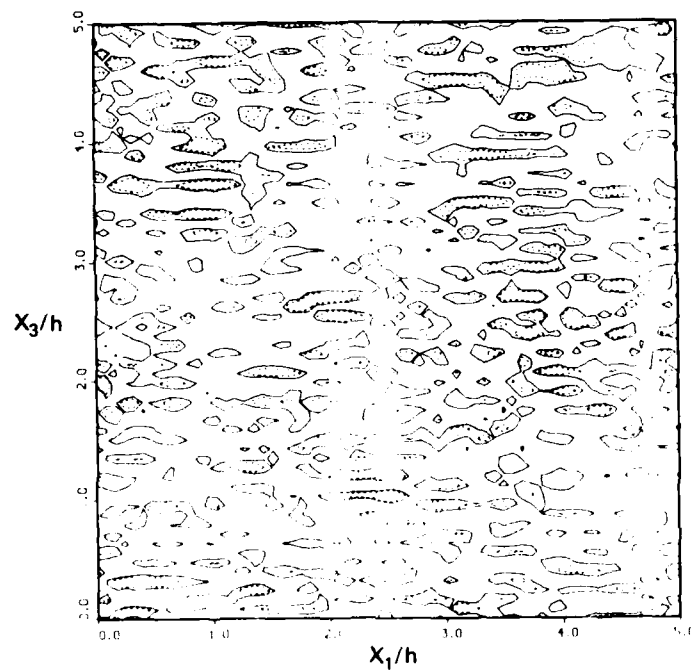


(d)  $x_2^* = 94.75$ .

Fig. 2 — (Continued) Contours of constant streamwise velocity. Contour levels are given by: — — — — —,  $(u_1 - \langle u_1 \rangle_h) - u_1^{rms}$ , — — — — —,  $(u_1 - \langle u_1 \rangle_h) - (.25 \times u_1^{rms})$ .

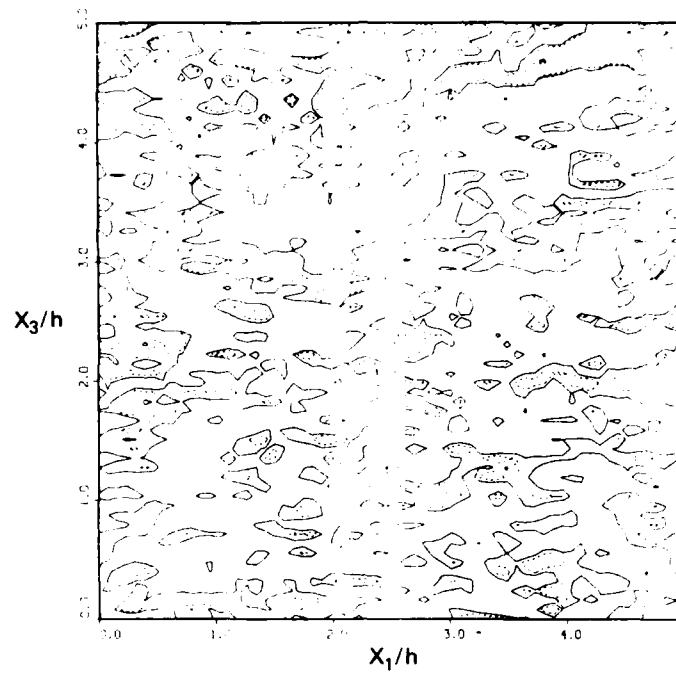


(a)  $x_2^* = 2.11$

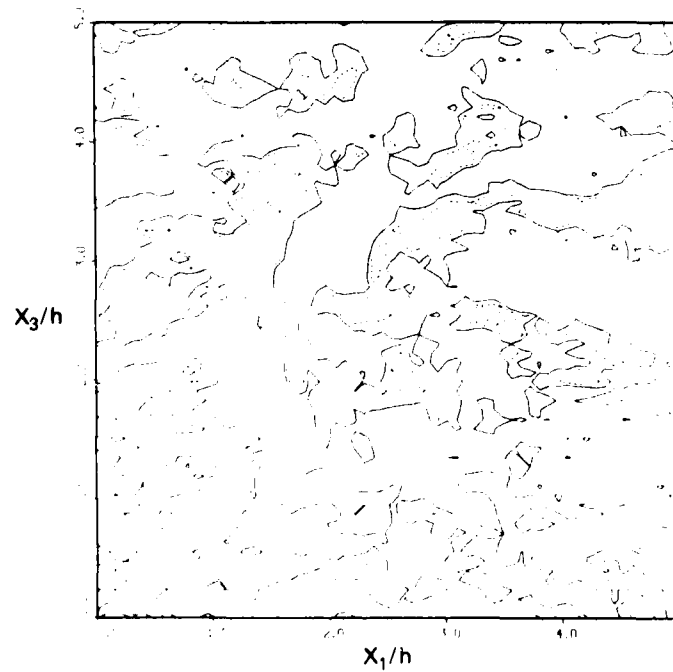


(b)  $x_2^* = 5.84$

Fig. 3 — Contours of constant wall normal velocity. Contour levels given by: — — —  $(u_2 + u_2^{rms})$ , —  $(u_2 + .25 \times u_2^{rms})$ .

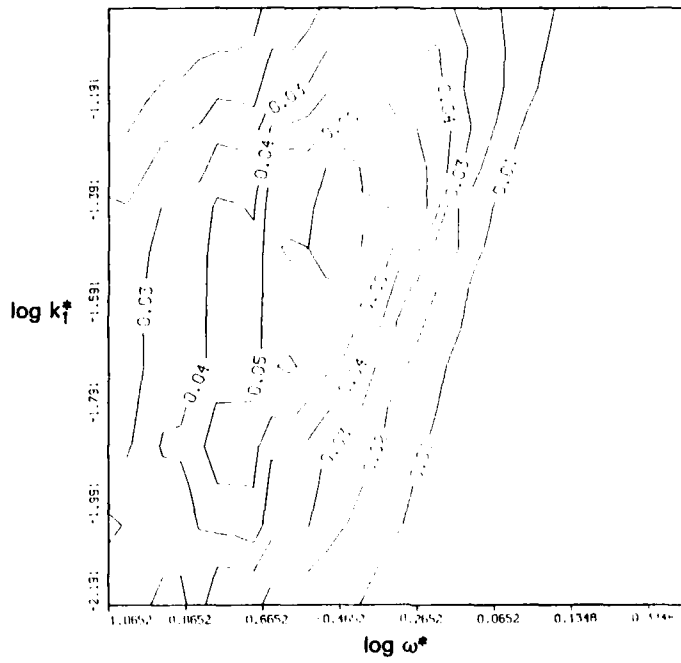


(c)  $x_2^* = 27.74$

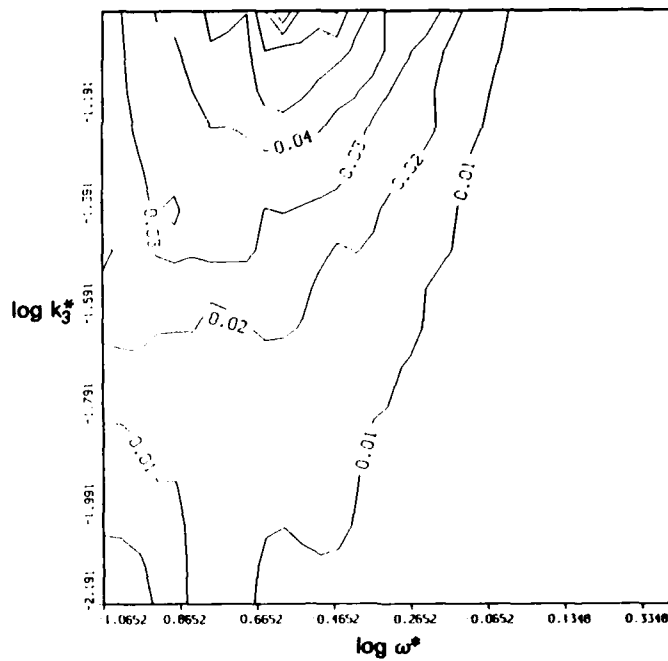


(d)  $x_2^* = 94.75$

Fig. 3 -- (Continued) Contours of constant wall normal velocity. Contour levels given by: ---  $(u_2 + u_2^{rms})$ , —  $(u_2 + .25 \times u_2^{rms})$ .

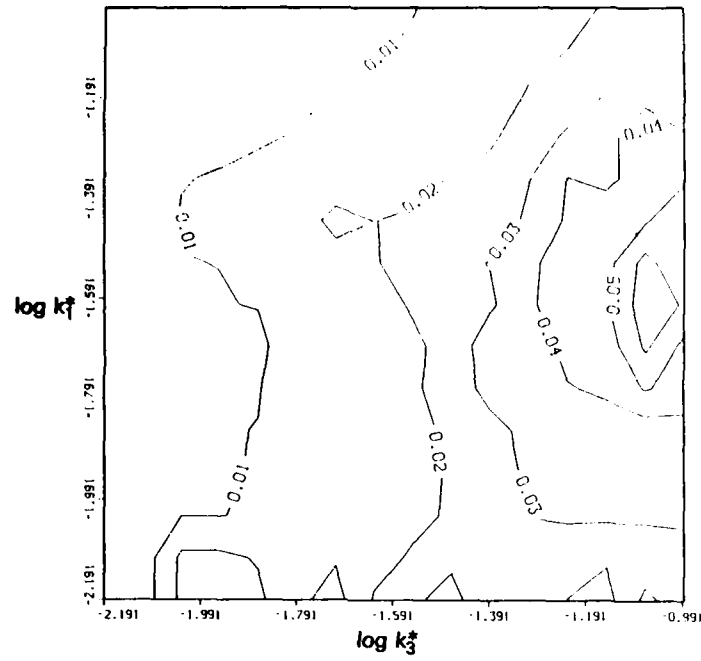


(a)  $\Lambda_{11}(k_1^*, \omega^*)$ ,  $x_2^* = 5.84$

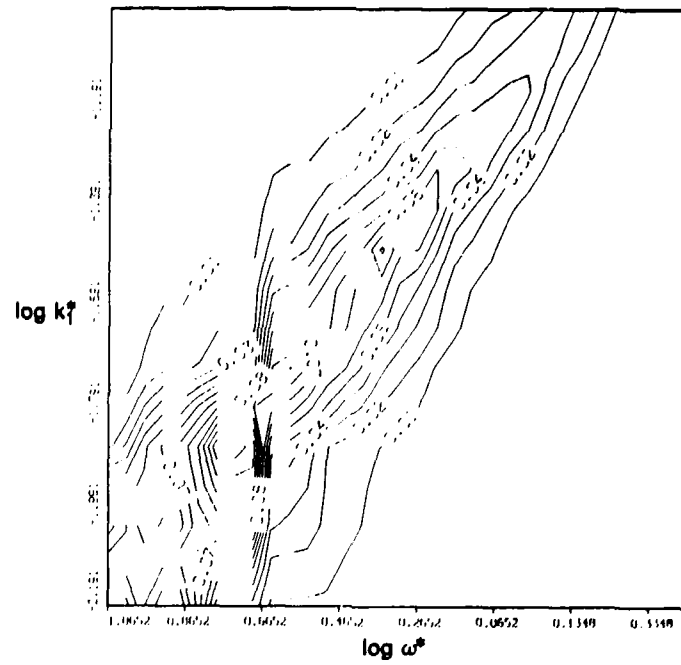


(b)  $\Lambda_{11}(k_3^*, \omega^*)$ ,  $x_2^* = 5.84$

Fig. 4 — Wavenumber-frequency spectra of the streamwise velocity.

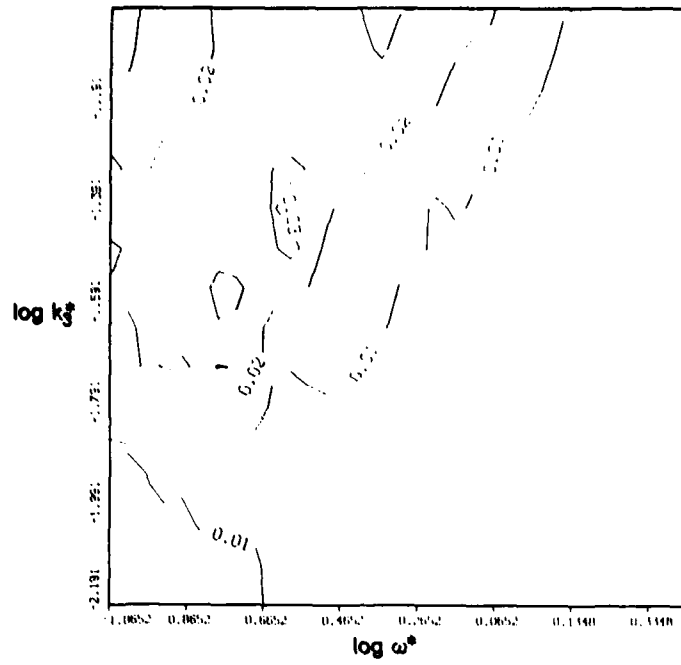


(c)  $A_{11}(k_3^*, k_1^*)$ ,  $x_2^* = 5.84$

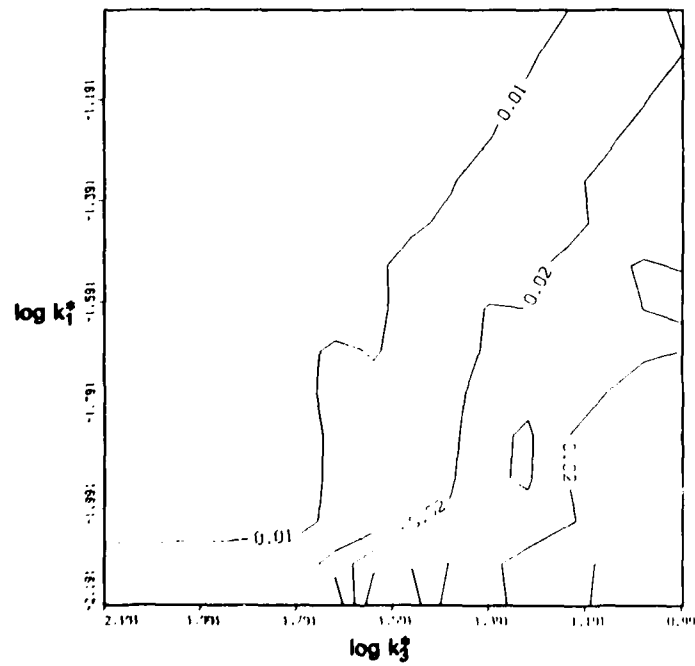


(d)  $A_{11}(k_1^*, \omega^*)$ ,  $x_2^* = 27.7$

Fig. 4 — (Continued) Wavenumber-frequency spectra of the streamwise velocity.

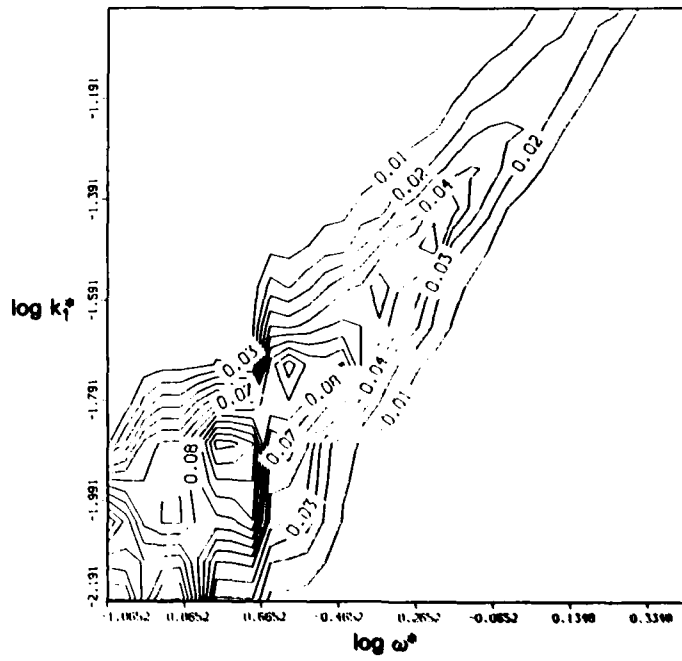


(c)  $\Lambda_{11}(k_3^*, \omega^*), x_2^* = 27.7$

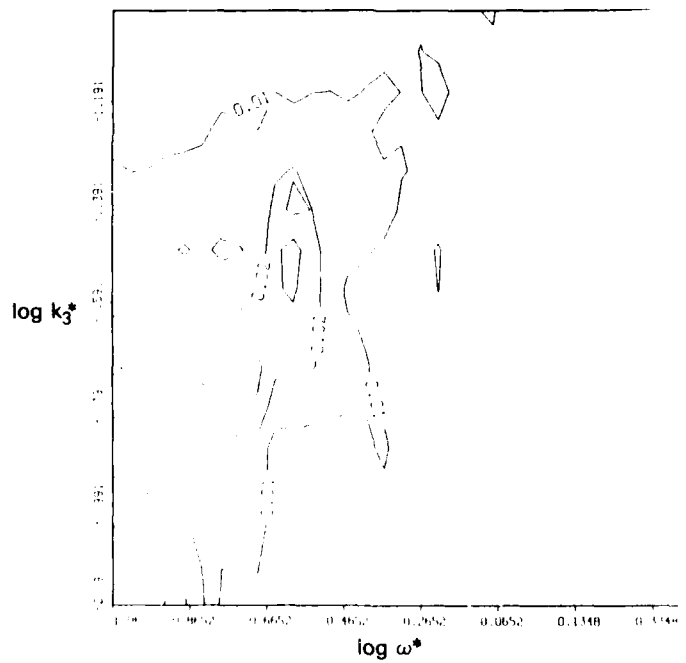


(f)  $\Lambda_{11}(k_3^*, k_1^*), x_2^* = 27.7$

Fig. 4 — (Continued) Wavenumber-frequency spectra of the streamwise velocity.

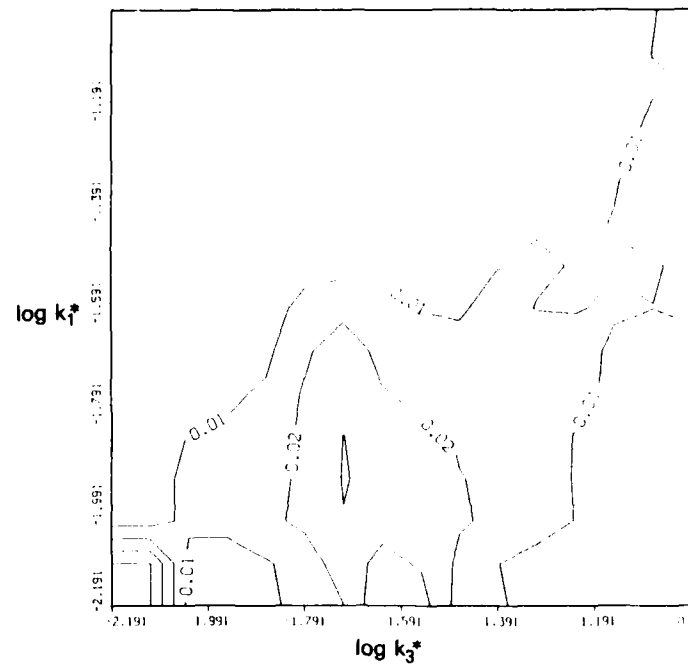


(g)  $\Lambda_{11}(k_1^*, \omega^*)$ ,  $x_2^* = 64.0$

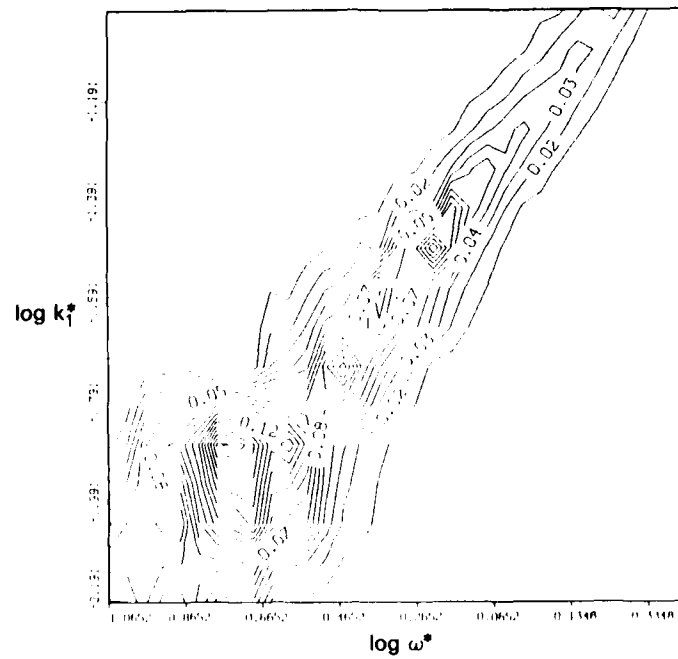


(h)  $\Lambda_{11}(k_3^*, \omega^*)$ ,  $x_2^* = 64.0$

Fig. 4 — (Continued) Wavenumber-frequency spectra of the streamwise velocity.

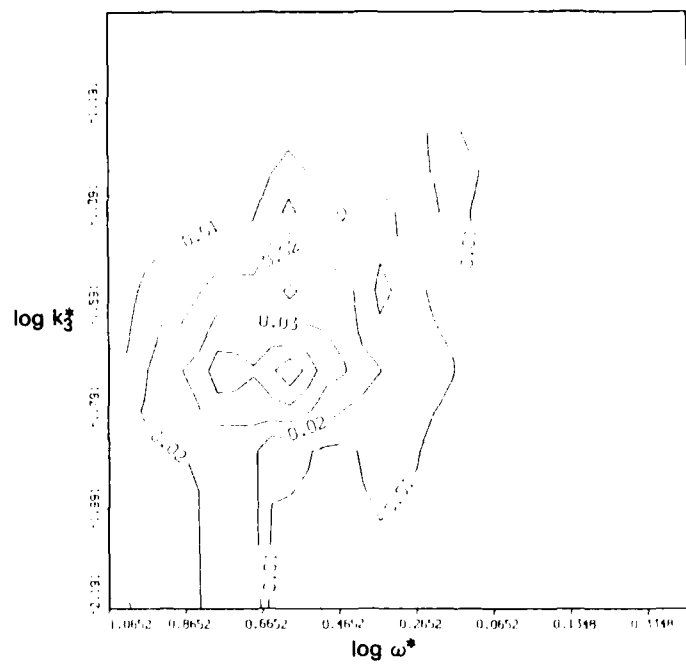


(i)  $\Lambda_{11}(k_3^*, k_1^*)$ ,  $x_2^* = 64.0$

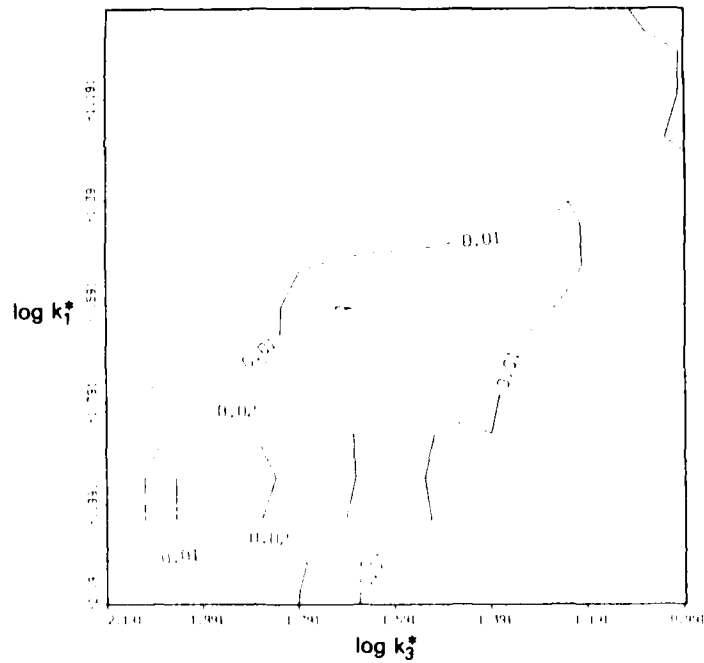


(j)  $\Lambda_{11}(k_1^*, \omega^*)$ ,  $x_2^* = 166.4$

Fig. 4 — (Continued) Wavenumber-frequency spectra of the streamwise velocity.

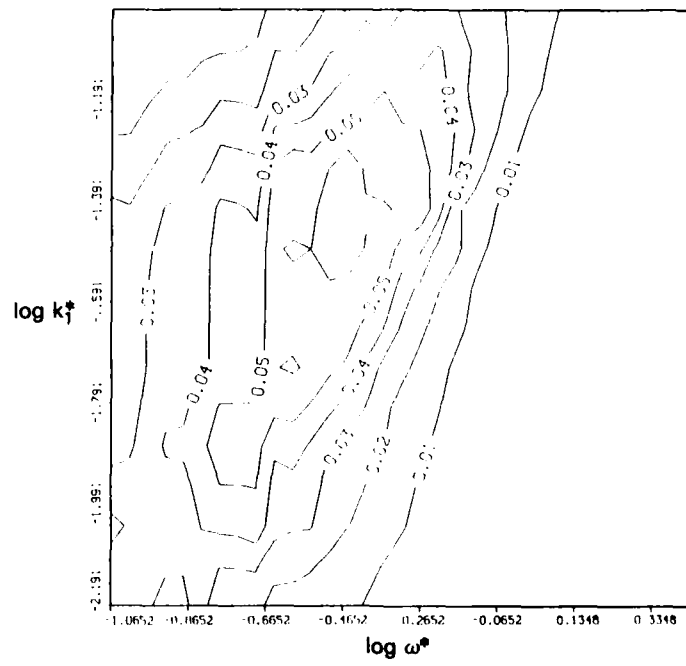


(k)  $\Lambda_{11}(k_3^*, \omega^*), x_2^* = 166.4$

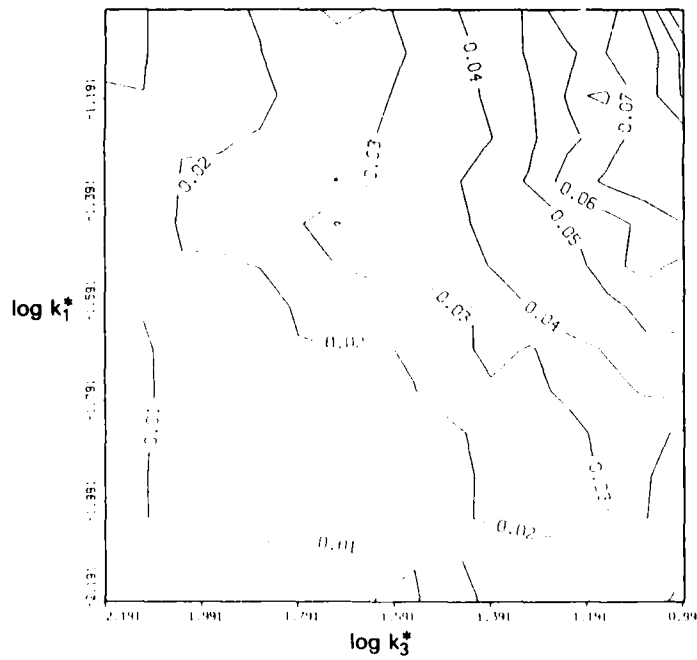


(l)  $\Lambda_{11}(k_3^*, k_1^*), x_2^* = 166.4$

Fig. 4 — (Continued) Wavenumber-frequency spectra of the streamwise velocity.

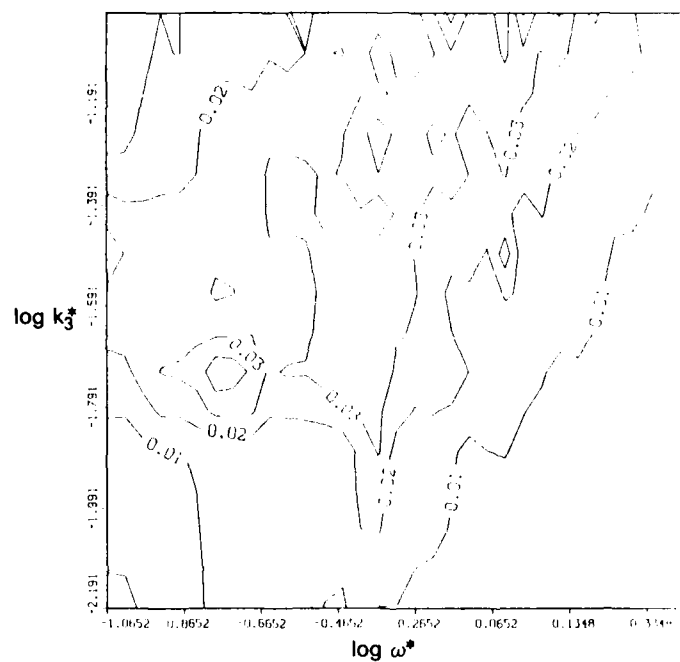


(a)  $\Lambda_{22}(k_3^*, \omega^*), x_2^* = 11.4$

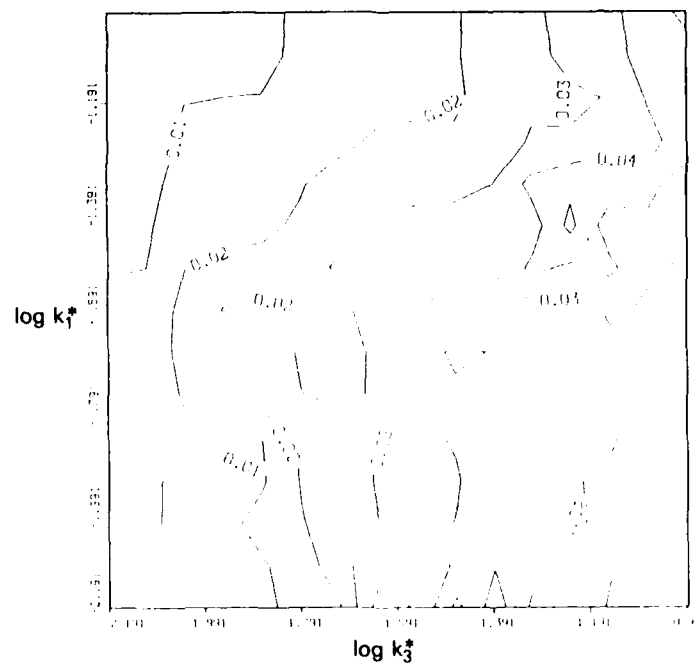


(b)  $\Lambda_{22}(k_3^*, k_1^*), x_2^* = 11.4$

Fig. 5 — Wavenumber- Frequency spectra of the wall normal velocity.

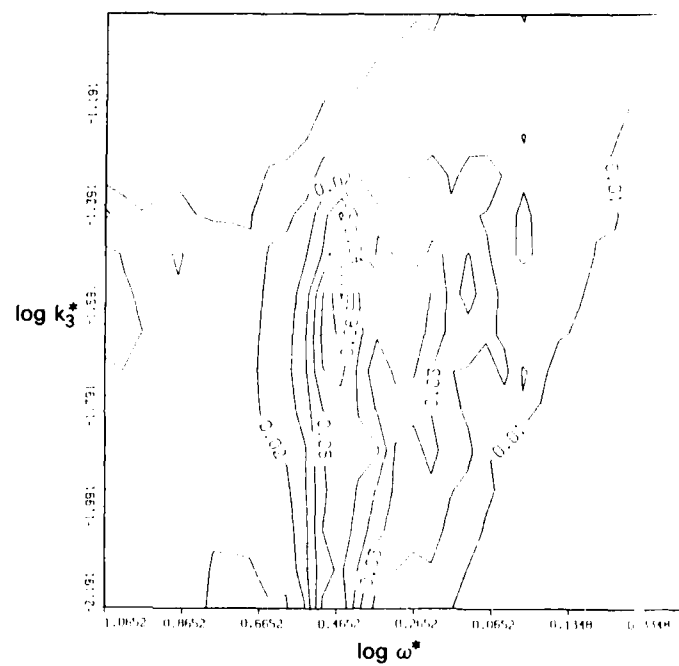


(c)  $\Lambda_{22}(k_3^*, \omega^*), x_2^* = 64.0$

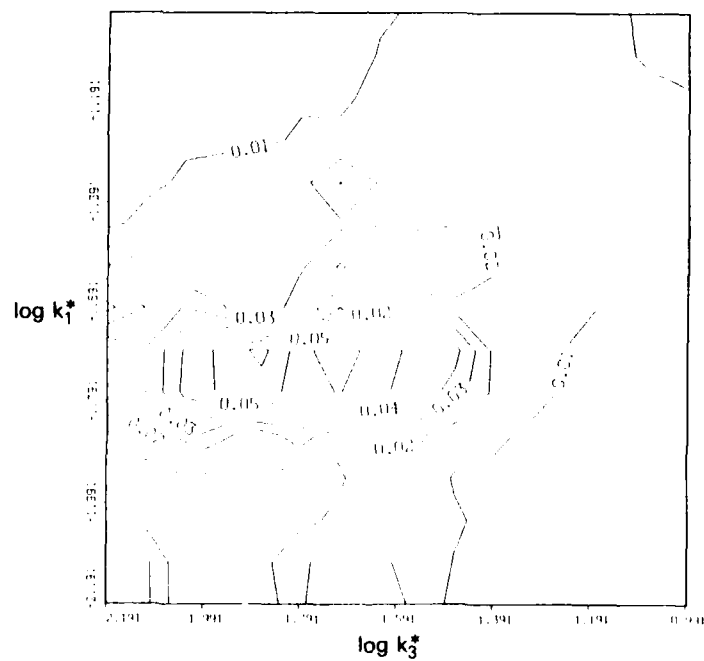


(d)  $\Lambda_{22}(k_3^*, k_1^*), x_2^* = 64.0$

Fig. 5 — (Continued) Wavenumber- Frequency spectra of the wall normal velocity.



(e)  $\Lambda_{22}(k_3^*, \omega^*), x_2^* = 166.4$



(f)  $\Lambda_{22}(k_3^*, k_1^*), x_2^* = 166.4$

Fig. 5 — (Continued) Wavenumber- Frequency spectra of the wall normal velocity.

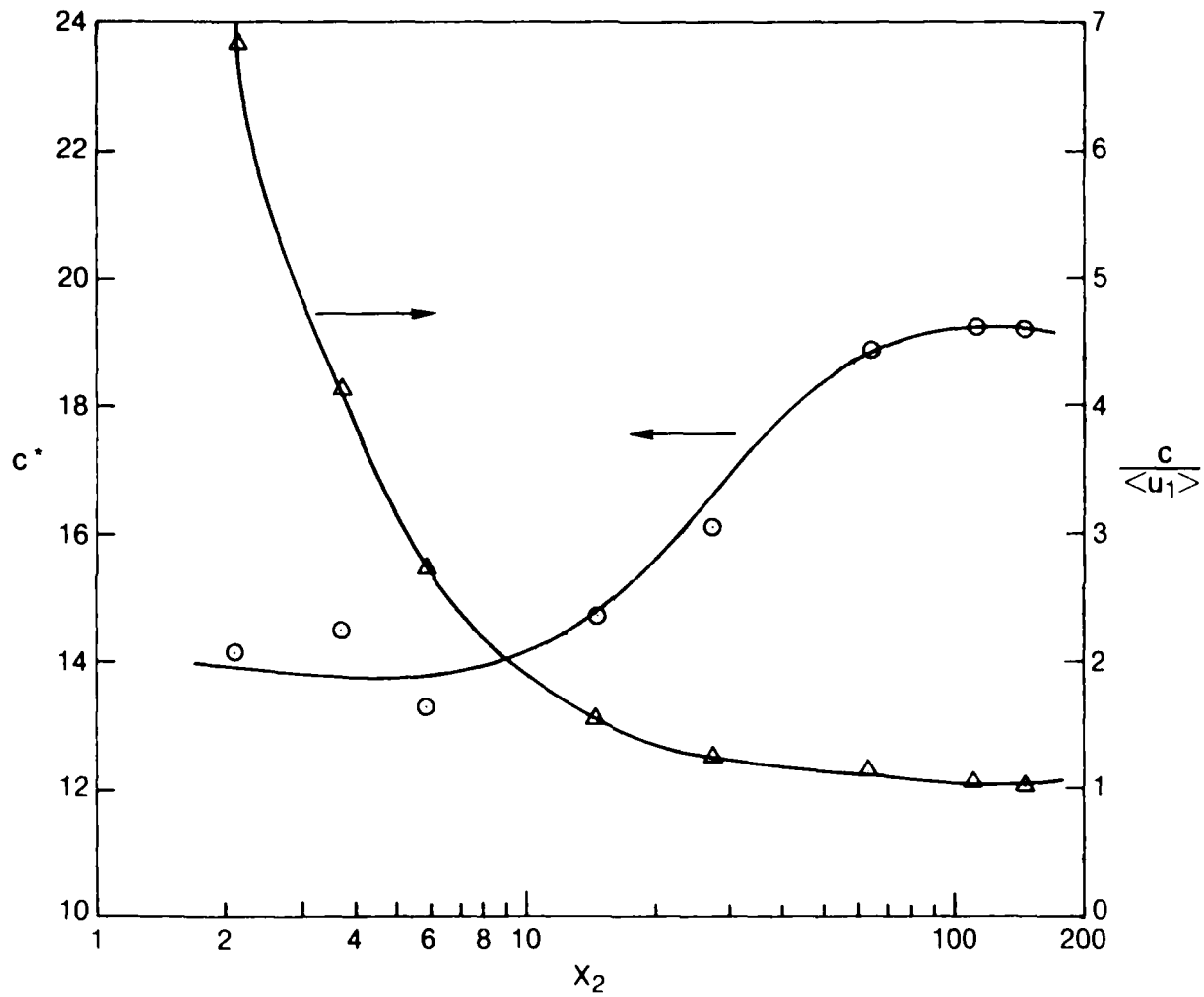
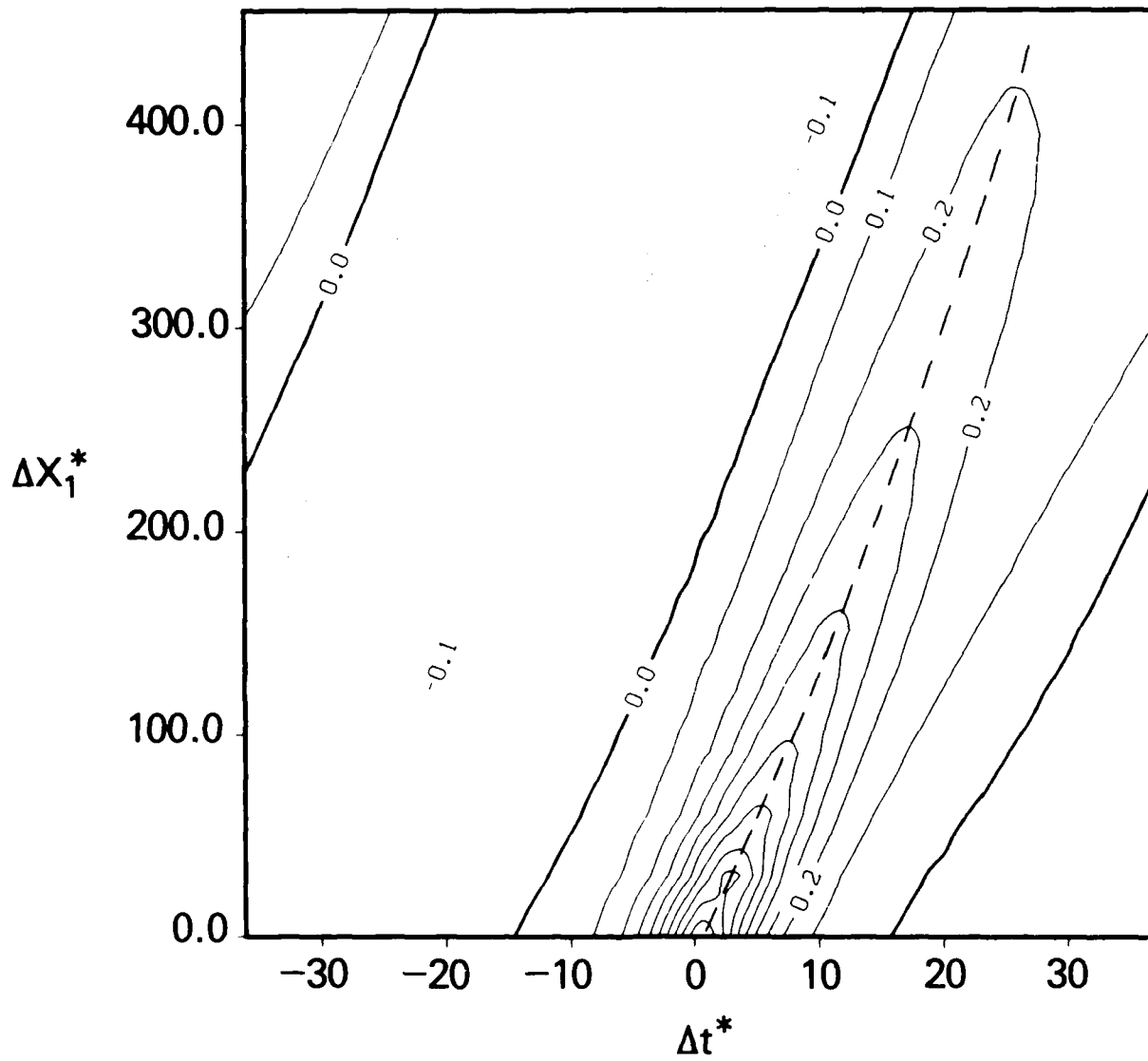
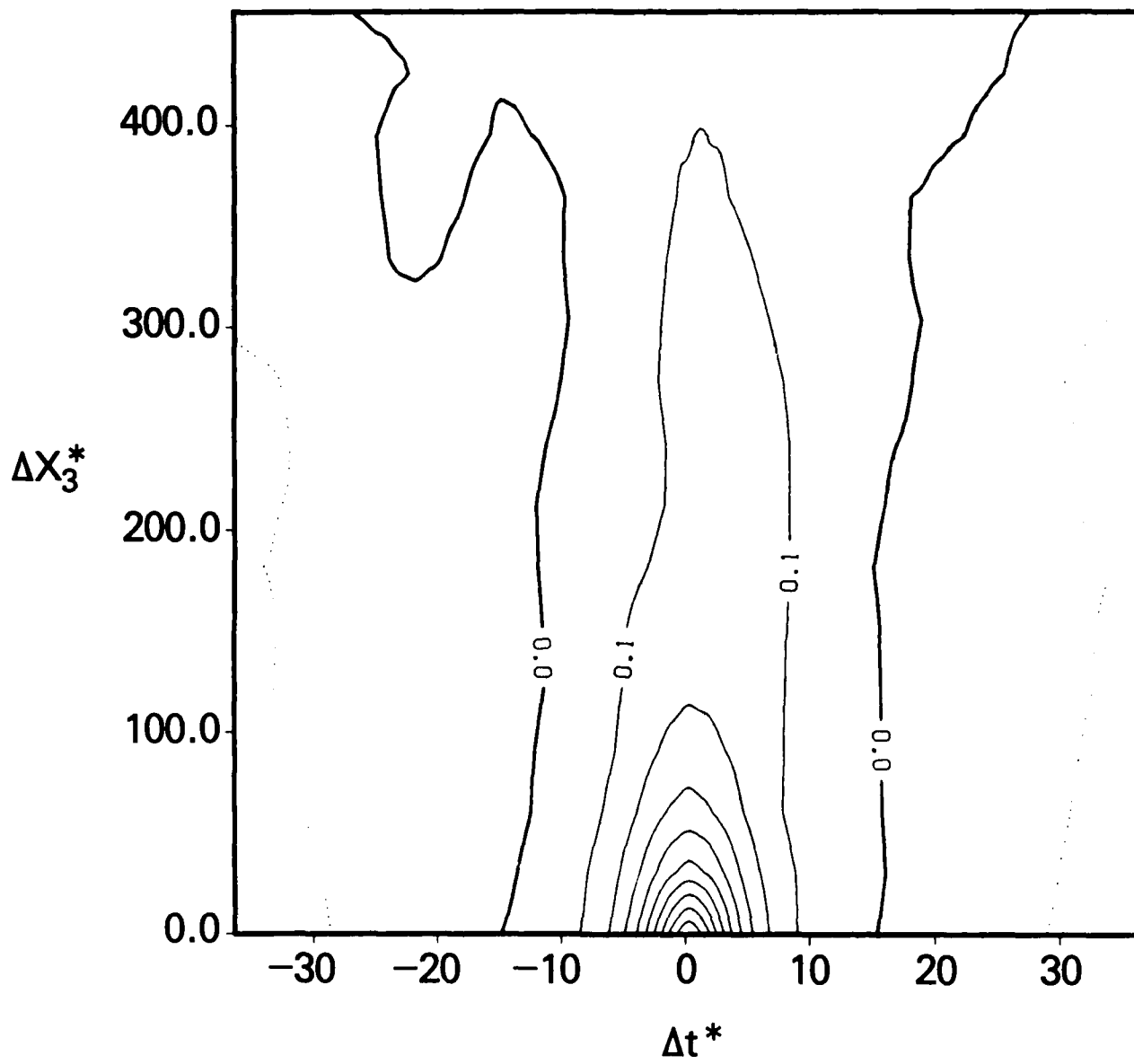


Fig. 6 - Wave speeds of the streamwise velocity fluctuations.  
 $\circ, c^*$ ;  $\Delta, c/\langle u_1 \rangle$



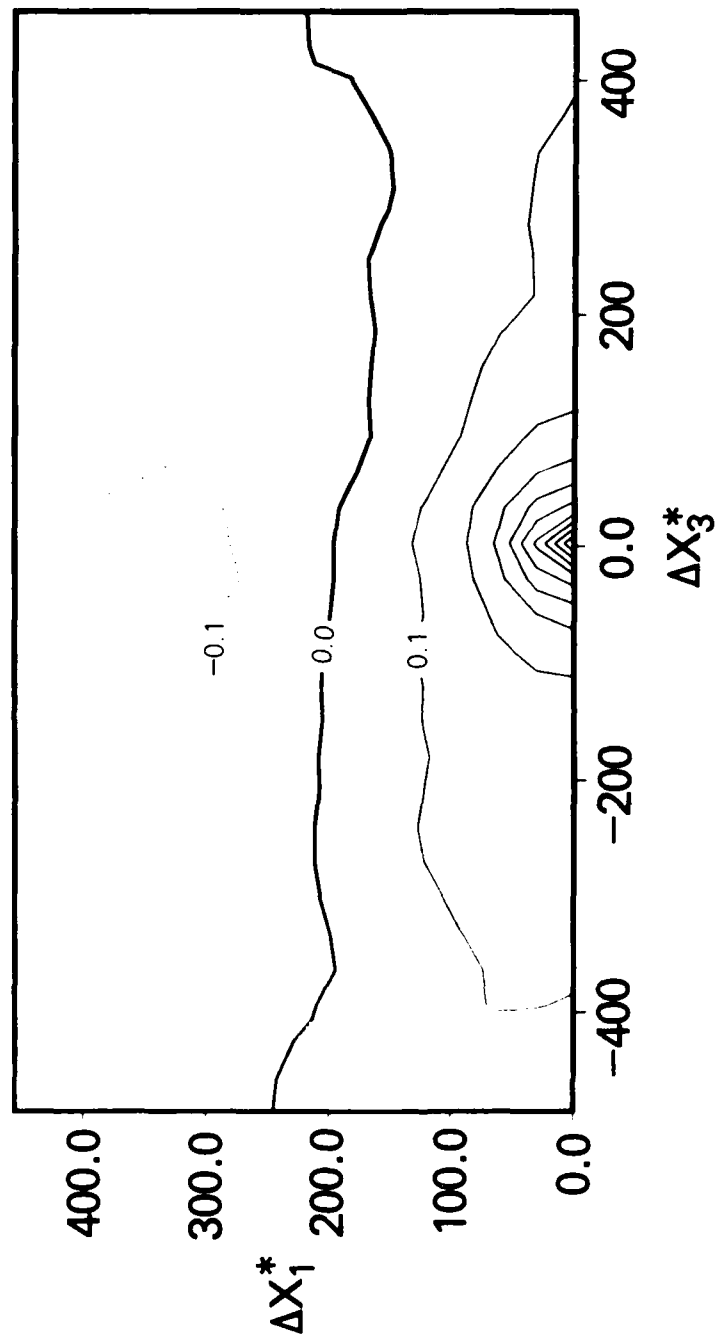
(a)  $R_{pp}(\Delta x_1^*, \Delta t^*)$

Fig. 7 - Space-time correlation function for the wall pressure field.

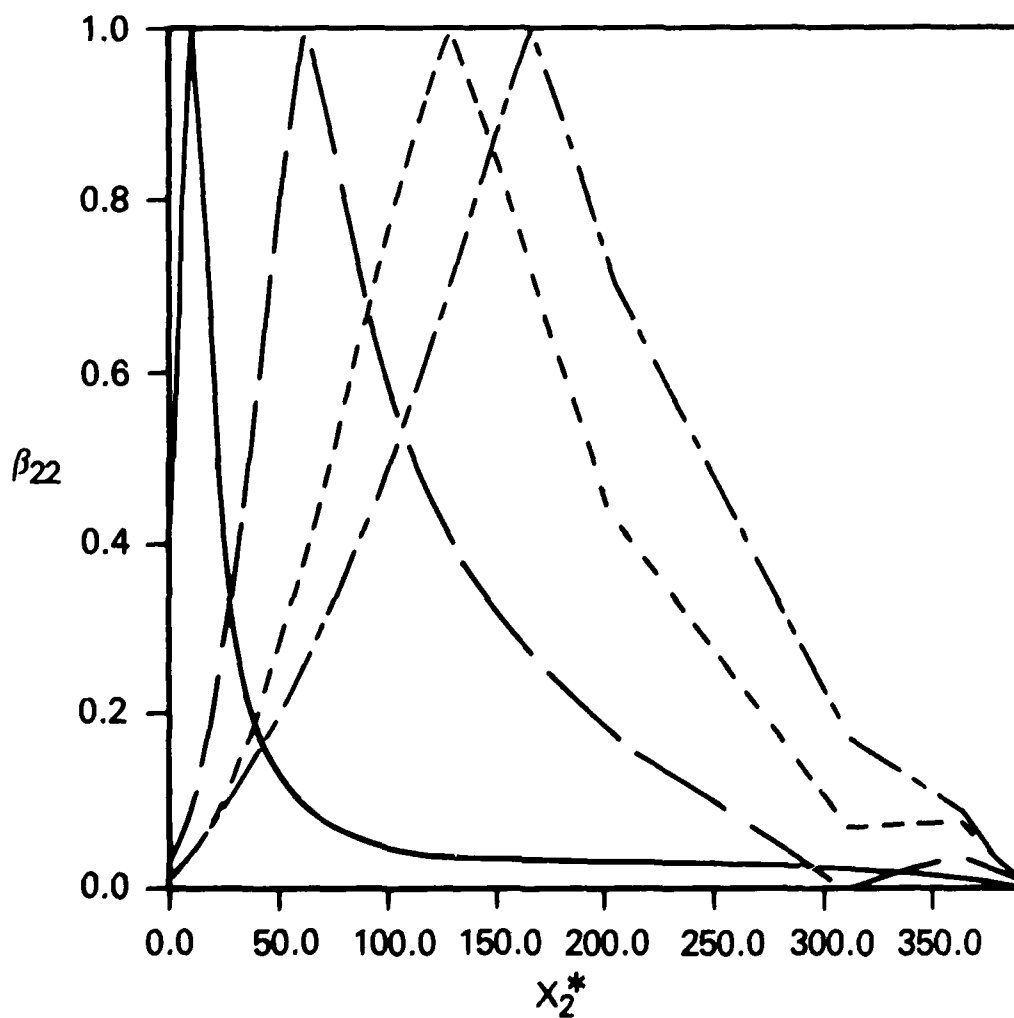


(b)  $R_{pp}(\Delta x_3^*, \Delta t^*)$

Fig. 7 — (Continued) Space-time correlation function for the wall pressure field.

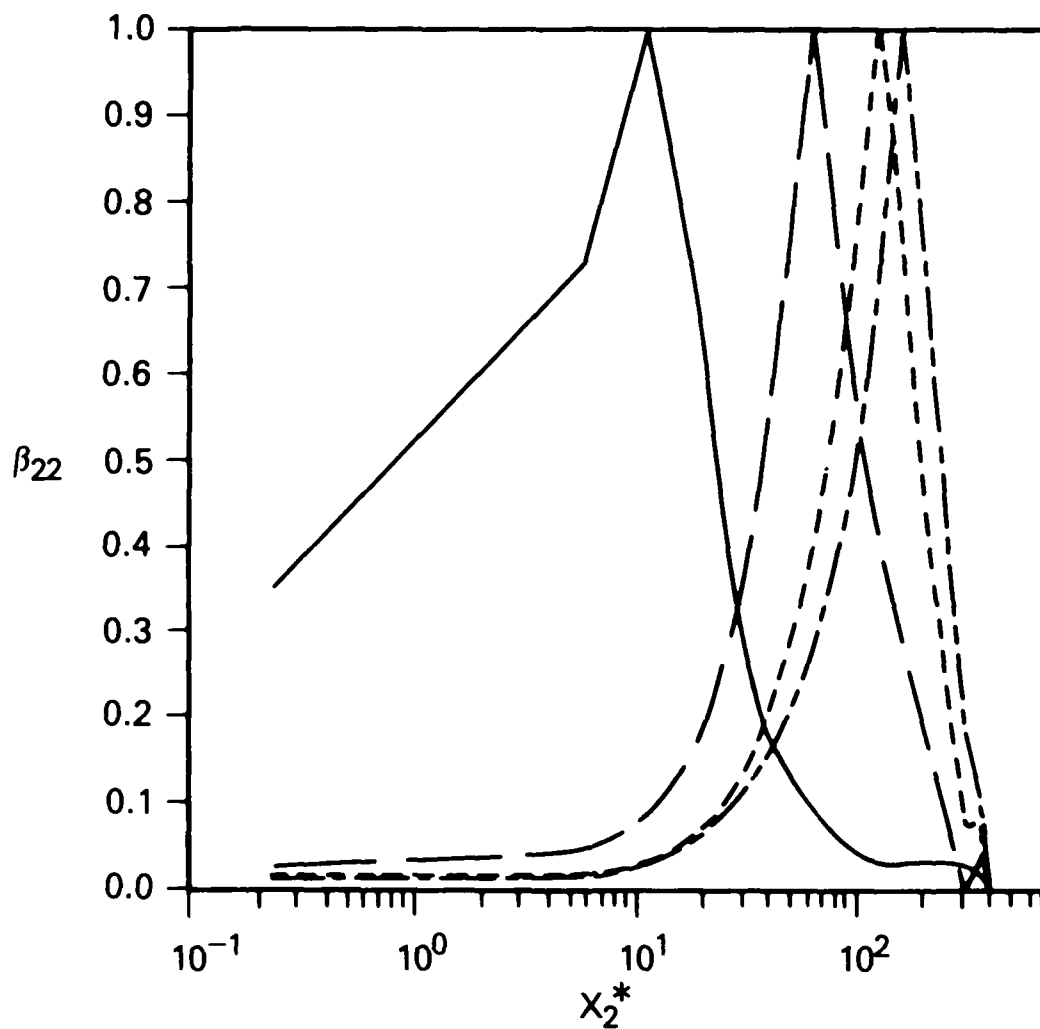


(c)  $R_{pp}(\Delta x_3^*, \Delta x_1^*)$   
 Fig. 7 — (Continued) Space-time correlation function for the wall pressure field.



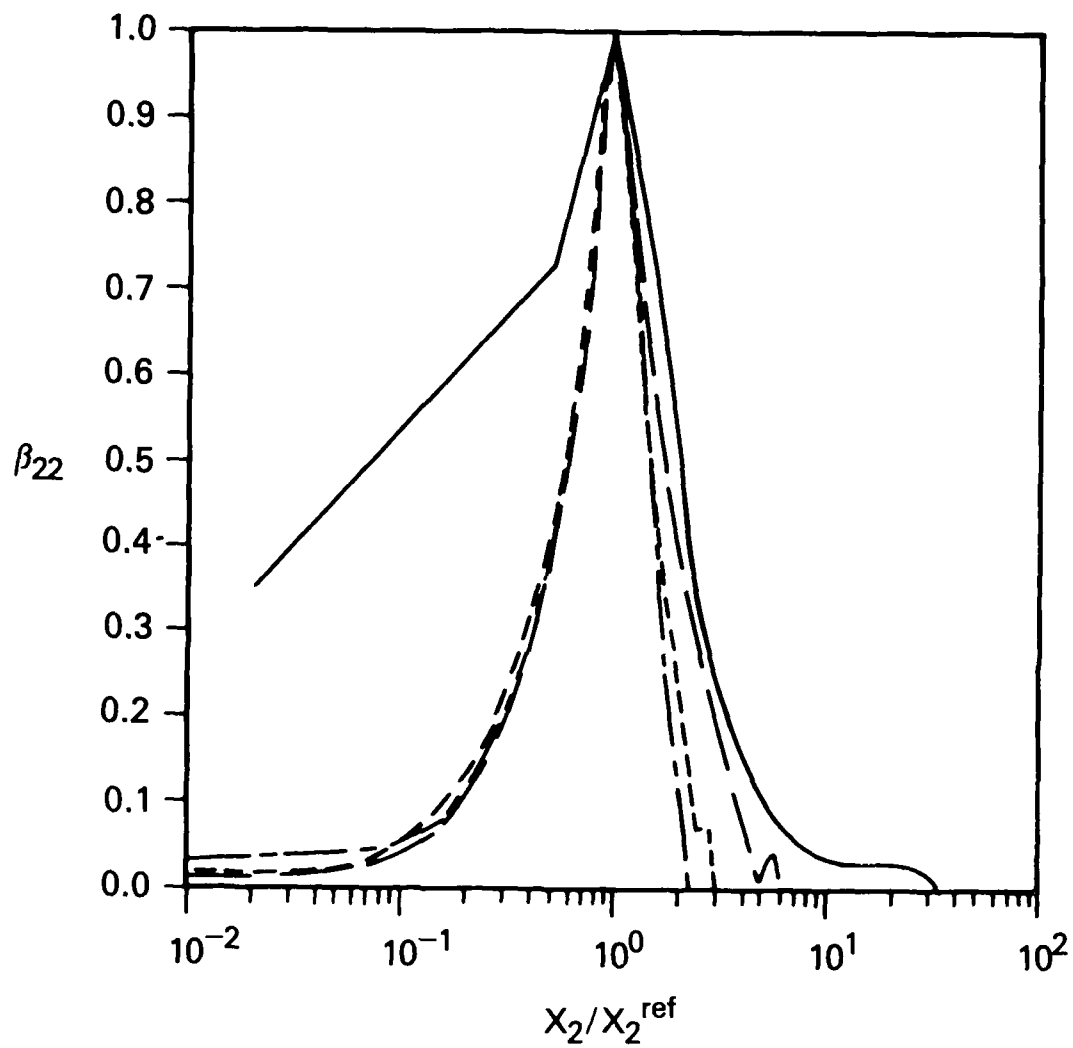
(a)  $\beta_{22}$ , linear scale

Fig. 8 — Broadband correlation function for the wall-normal velocity. Reference distances from the wall in viscous units, —, 11.4, — —, 64.0, — — —, 129.31, — · —, 166.39.



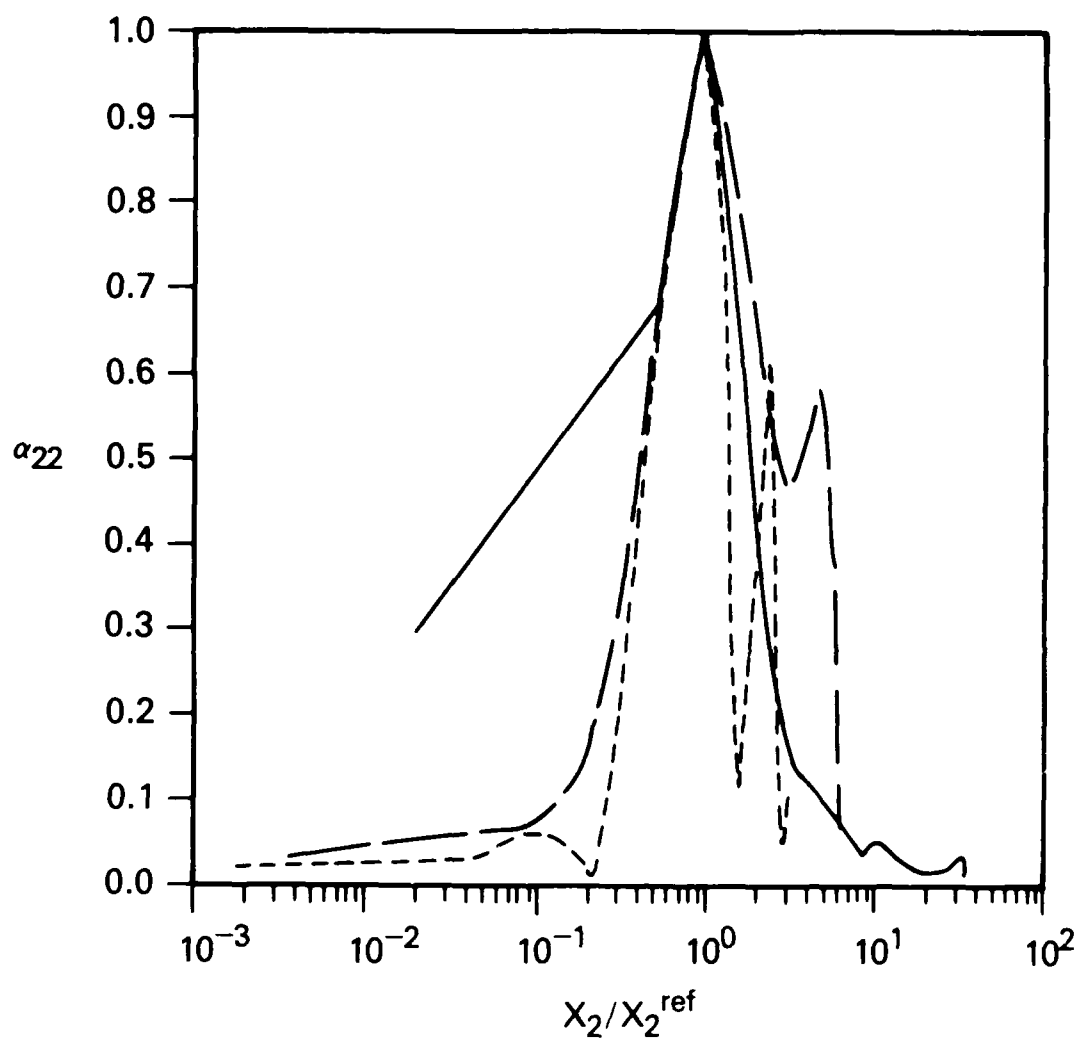
(b)  $\beta_{22}$ , logarithmic scale

Fig. 8 — (Continued) Broadband correlation function for the wall-normal velocity. Reference distances from the wall in viscous units, —, 11.4, — —, 64.0, — — —, 129.31, — — — —, 166.39.



(c)  $\beta_{22}$ , versus nondimensional wall distance.

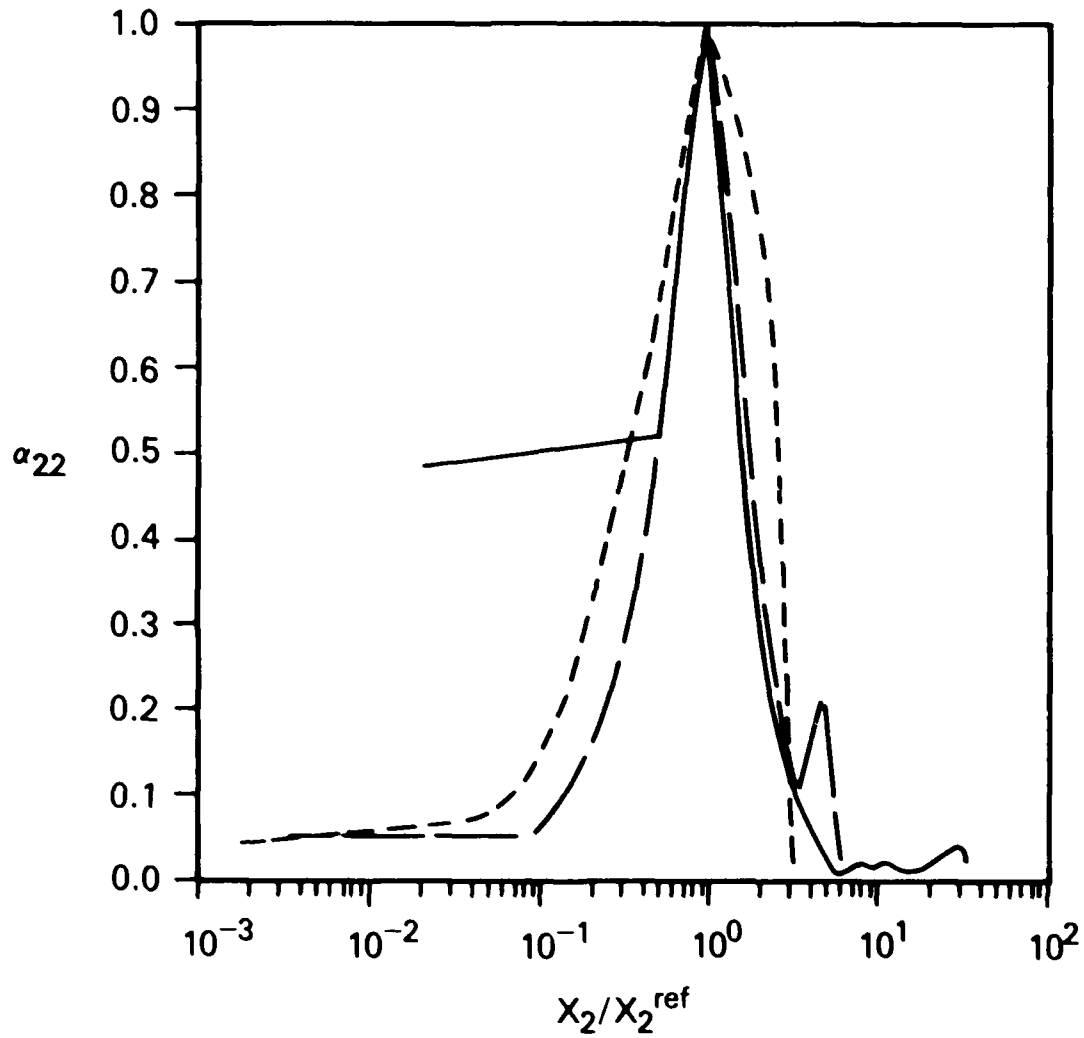
Fig. 8 — (Continued) Broadband correlation function for the wall-normal velocity. Reference distances from the wall in viscous units, —, 11.4, — —, 64.0, — — —, 129.31, — · —, 166.39.



(a)  $\omega x_2^{ref}$ , (in viscous units):

—, 10.79, - - -, 11.02, - · - ·, 11.13.

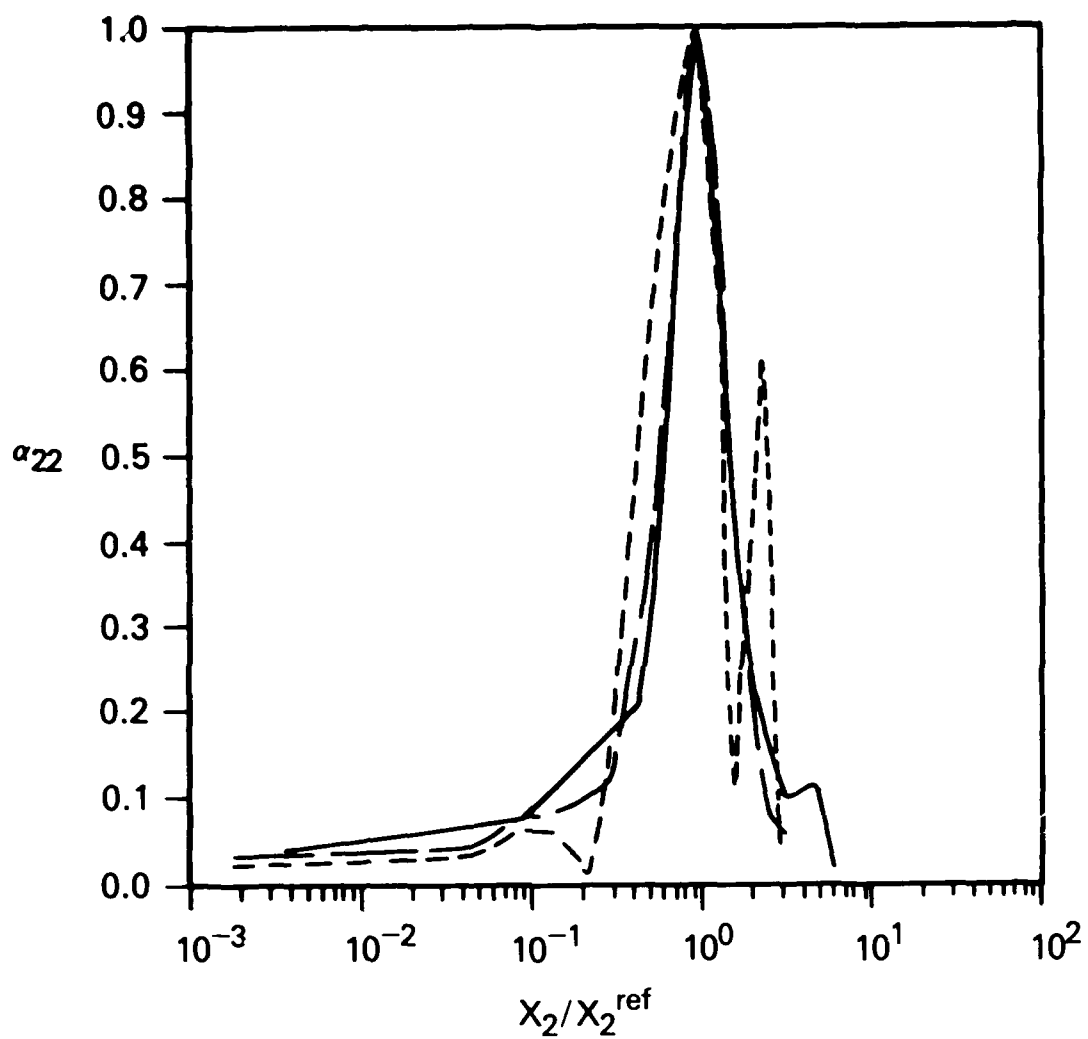
Fig. 9 — Narrowband correlation function of the wall-normal velocity.



(b)  $\omega x_2^{ref}$ , (in viscous units):

—, 10.79, - - -, 11.02, — · —, 11.13.

Fig. 9 (Continued) Narrowband correlation function of the wall-normal velocity.



(c)  $\omega x_2^{ref}$ , (in viscous units):

—, 10.79, — —, 11.02, — — —, 11.13.

Fig. 9 — (Continued) Narrowband correlation function of the wall-normal velocity.

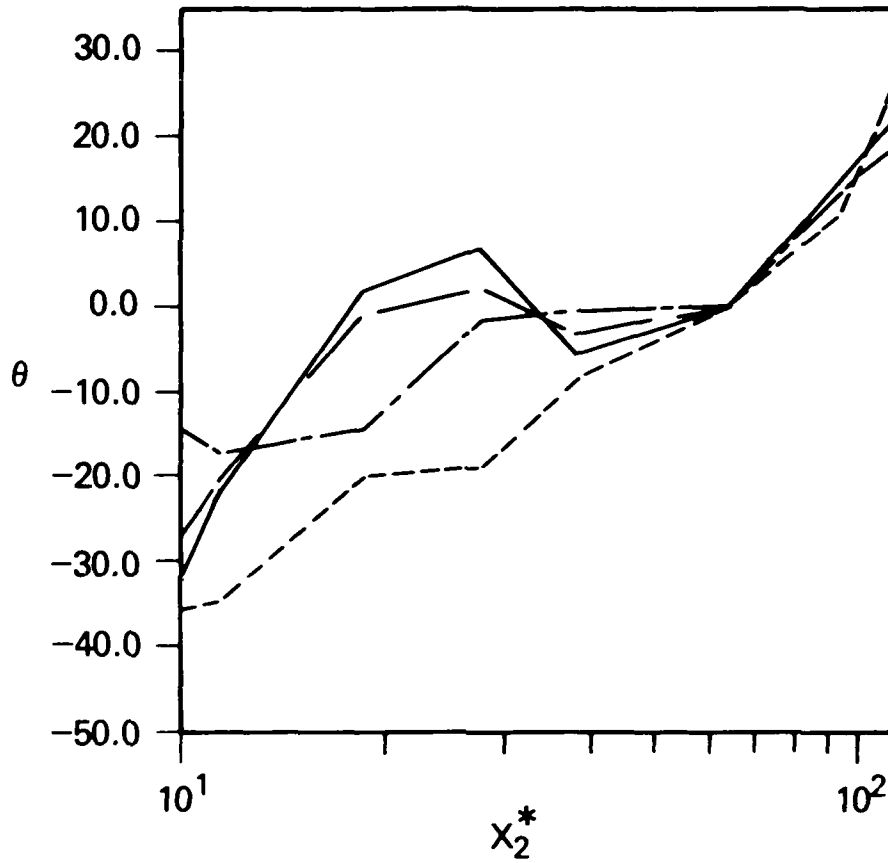


Fig. 10 — Phase change (in degrees).  $x_2^{*cf} = 64.05$  (in viscous units).  
 $\omega^* = \text{---}, 0.602, \text{---}, 1.03, \text{---}, 1.46, \text{---}, 1.89$ .

END

DATE

FILMED

MARCH

1988

DTIC